

Trapped waves in supersonic and hypersonic turbulent channel flow over porous walls

Yongkai Chen^{1,†} and Carlo Scalo^{1,2}

¹School of Mechanical Engineering, Purdue University, West Lafayette, IN 47906, USA

²School of Aeronautics and Astronautics, Purdue University, West Lafayette, IN 47906, USA*

(Received 28 October 2020; revised 2 May 2021; accepted 13 May 2021)

This study investigates the effect of an isothermal wall with complex impedance on compressible turbulent channel flow up to bulk Mach numbers of 6.00. Such investigation is carried out via the time-domain impedance boundary conditions based on auxiliary differential equations method. A three-parameter complex impedance, modelling a frequency-selective porous wall, with tuneable resonating frequency ω_{res} and variable resistance $R \in [0.10, 1.0]$ is employed. Higher resistance leads to lower wall permeability with $R \rightarrow \infty$ representing the impermeable limit. Three bulk Mach numbers $M_b = \{1.50, 3.50, 6.00\}$ are investigated with a semi-local Reynolds number $Re_\tau^* \approx 220$. It is found that a sufficiently low R could trigger flow instabilities, which comprise streamwise-travelling waves in the near-wall region, akin to spanwise rollers at low subsonic flow conditions and second-mode waves at hypersonic conditions. The probability density function of instantaneous wall-shear stress shows an enhancement in extreme positive cases of wall-shear stress fluctuations, leading to an increase in the mean wall-shear stress due to porous walls. The wave dynamically affects the turbulence, yielding a local peak near the wall in the pre-multiplied spectrum of the production term of turbulence kinetic energy. Linear stability analysis using the turbulent base flow profile confirmed that the finite wall permeability triggers the instability when R is below a threshold R_{cr} , which shows a sub-linear proportionality on the bulk Mach number M_b . The perturbed field exhibits more dilatational nature in high Mach number flows with low permeability.

Key words: high-speed flow, compressible turbulence, instability control

1. Introduction

1.1. Impedance boundary conditions (IBCs)

When performing numerical simulations of flow over porous walls, including the geometry of the pores directly in the computational domain requires a significantly

[†] Email address for correspondence: chen1305@purdue.edu

* The online version of this article has been updated since original publication. A notice detailing the change has also been published

higher computation effort as compared with simulations over a smooth impermeable wall, especially in the case of distributed small-scale porosity, typically found in supersonic and hypersonic applications (Wagner 2014; Sousa *et al.* 2019). An alternative is to define wall boundary conditions that can accurately mimic the interaction between the porous wall and the overlying flow field. Such an approach dates back to the work done by Ingard (1959), who analytically derived the wall boundary condition of an inviscid flow grazing a plane porous boundary. Later, Myers (1980) extended the condition to account for arbitrary smooth wall shapes and mean flow directions. The two results together are usually referred to as the Ingard–Myers condition in the community. Both papers introduced the concept of wall impedance $\hat{Z}(\omega)$ (Kinsler *et al.* 1999)

$$\hat{Z}(\omega) = \frac{1}{\rho_s a_s} \frac{\hat{p}(\omega)}{\hat{\mathbf{v}}(\omega) \cdot \mathbf{n}} = \underbrace{R(\omega)}_{\text{resistance}} + i \underbrace{X(\omega)}_{\text{reactance}}, \quad (1.1)$$

where $\hat{p}(\omega)$ and $\hat{\mathbf{v}}(\omega)$ are the Fourier transform of the fluctuations of the instantaneous pressure and velocity at the impedance boundary; ω is the angular frequency; \mathbf{n} is the outward surface normal vector, i.e. pointing away from the flow side; $i = \sqrt{-1}$ is the imaginary unit; ρ_s and a_s are the base density and speed of sound with the subscript ‘s’ indicating quantities taken on the impedance surface. The real part of the impedance $R(\omega)$ is typically referred to as the resistance, while the imaginary part $X(\omega)$ is called the reactance. The impedance is defined in the Fourier domain and its time-domain equivalent $z(t)$ is needed when applying the condition for a time-domain-based problem. Such a condition is usually referred to as the time-domain impedance boundary condition (TDIBC) and will be introduced in the next subsection.

1.2. Time-domain impedance boundary conditions

If the pressure is treated as an unknown in (1.1), its time-domain expression involves a convolution integral, written as

$$p'(t) = \rho_s a_s \int_{-\infty}^{\infty} z(\tau) v'_n(t - \tau) d\tau, \quad (1.2)$$

where $p'(t)$ and $v'_n(t)$ are the pressure and surface normal velocity fluctuations in the time domain; alternatively, $v'_n(t)$ could be expressed as a convolution integral of pressure involving the inverse Fourier transform of $Z^{-1}(\omega)$. Implementing TDIBC in either form would require direct numerical evaluation of such a convolution integral. The TDIBC approach adopted in the current paper, however, does not directly impose $\hat{Z}(\omega)$ or $\hat{Z}^{-1}(\omega)$, but rather the wall softness $\hat{S}(\omega)$ adopting a characteristic-wave-based approach (see § 3). The latter only requires causality constraints on $\hat{S}(\omega)$ itself, and not directly on $Z(\omega)$ (Fung & Ju 2001, 2004; Scalo, Bodart & Lele 2015; Lin, Scalo & Hesselink 2016; Douasbin *et al.* 2018; Sousa *et al.* 2019).

In all cases, realizability constraints on the impedance boundary condition should be honoured. As clearly stated by Rienstra (2006) and summarized by Douasbin *et al.* (2018), a realizable impedance boundary condition in the form of (1.1) should satisfy the following conditions:

- (i) *Passivity of the boundary.* The impedance boundary should not emit acoustic energy on its own. Thus the net acoustic flux into the wall must always be non-negative,

which requires:

$$\operatorname{Re}\{\hat{Z}(\omega)\} \geq 0, \quad \forall \omega \in \mathbb{R}. \quad (1.3)$$

- (ii) *Reality of the signal.* Since the pressure and wall-normal velocity signals are purely real, the time-domain impedance $z(t)$ must be real, which implies

$$\hat{Z}(\omega) = \hat{Z}^*(-\omega), \quad (1.4)$$

where the superscript $*$ indicates the complex conjugate.

- (iii) *Causality.* A physical process should not depend on any information from the future, which requires $\hat{Z}(\omega)$ and $\hat{Z}^{-1}(\omega)$ to satisfy conditions that guarantee their respective convolution integrals be causal in time.

Failing to satisfy the above constraints might result in inaccurate physical predictions. Early in 1973, Tester (1973) performed a detailed analysis of the acoustic field in a quasi-one-dimensional inviscid flow. It was shown that, in a particular example, one mode can grow along the streamwise direction. This mode is related to a modified version of Kelvin–Helmholtz instability, caused by the vanishing boundary layer thickness (and thus the thin vortex sheet) when applying the inviscid Ingard–Myers condition. Such instability was later shown by Brambley (2009) to admit arbitrary large growth rates in the frequency domain for various types of impedance models, and the corresponding time-domain problem is then ill posed in the sense of Hadamard. However, a well-posed problem can be obtained when a finite thickness boundary layer is considered, as shown by Rienstra & Darau (2011). The current work focuses on the latter case, in which the effects of applying TDIBCs to fully turbulent supersonic and hypersonic boundary layer types of flows are analysed. Despite the fact that instability could be the result of the ill posedness, there is experimental evidence that a Kelvin–Helmholtz instability can develop in the scenario of non-zero mean flow over a porous wall (see Brandes & Ronneberger 1995; Aurégan, Leroux & Pagneux 2005; Aurégan & Leroux 2008; Marx *et al.* 2010). Hence, avoiding numerical instabilities is important to not obfuscate the actual physical phenomena, which requires the construction of appropriate impedance boundary conditions. For this purpose, Tam & Auriault (1996) proposed a method based on a three-parameter impedance model applied to linearized Euler equations. In this work, harmonic forms of pressure and flow velocity were assumed and a set of time-domain ordinary differential equations (ODEs) were derived directly from their Fourier-domain counterpart. It was mathematically proven that, as long as the imaginary part of the impedance model has either non-negative mass-like reactance or negative spring-like reactance (while using the $e^{-i\omega t}$ convention), the causality is guaranteed and the resulting TDIBC leads to a well-posed problem. Other techniques such as z -transform has also been adopted to derive the numerical implementation of TDIBC, as done by Özyörük & Long (1997) and Özyörük, Long & Jones (1998). The property of z -transform allows a direct numerical formulation of TDIBC when the complex impedance model is given in rational form, as is usually done in digital filter design. The TDIBC can also be applied via residue theorem, as shown by Fung & Ju (2001, 2004). Instead of using pressure and wall-normal velocities, this method is constructed via the domain leaving wave $\hat{v}_n^{out}(\omega)$ and the domain entering wave $\hat{v}_n^{in}(\omega)$, related via wall softness $\hat{S}(\omega) = 2/[1 + \hat{Z}(\omega)]$, that is, $\hat{v}_n^{in}(\omega) = [\hat{S}(\omega) - 1]\hat{v}_n^{out}(\omega)$. The convolution integral deduced from (1.2) is then evaluated with the residue theorem. However, the method is limited to second-order temporal accuracy. To address this issue, Dragna, Pineau & Blanc-Benon (2015), Troian *et al.* (2017) replaced the convolution integral with a set of auxiliary variables, each governed by a first-order ODE. This method

is usually referred to as the auxiliary differential equation (ADE) method that originates from the field of electromagnetism (Joseph, Hagness & Taflove 1991). The method used in this paper is built upon the ADE formulation. One big advantage of the ADE method is that it can go up to an arbitrary order of accuracy and allows easy coupling with the flow solver.

1.3. Applications of TDIBC to flows over porous walls

TDIBCs have been applied to different flow problems ranging from subsonic turbulent flows to transitional hypersonic boundary layers. In low-speed applications, TDIBCs are mainly used to investigate how the acoustic liners affect the overlying flow fields. For example, Jiménez *et al.* (2001) performed direct numerical simulations (DNS) of incompressible plane turbulent channel flow over a bottom porous wall. It is important to clarify that, in this work, the impedance is purely real, taking the form $v'_n = -\beta p'$, where β is the permeability that finds its counterpart in R^{-1} in the current study. To the authors' knowledge, the first work to apply TDIBC to model compressible subsonic flow over porous walls is the one by Scalo *et al.* (2015), which adopts the three-parameter impedance model by Tam & Auriault (1996) and TDIBC formulation by Fung, Ju & Tallapragada (2000). This manuscript extends the work of Scalo *et al.* (2015) to the supersonic and hypersonic regimes. The tuneable resonating frequency ω_{res} of the three-parameter impedance is set to match the most energetic flow frequency, as also done in Scalo *et al.* (2015). As discussed in this manuscript, the type of response observed in the supersonic and hypersonic regimes is more dilatational in nature than the (more hydrodynamic) instability seen in Scalo *et al.* (2015). Olivetti, Sandberg & Tester (2015) applied the same three-parameter impedance model, however, using the ODE form of TDIBC derived by Tam & Auriault (1996) to simulate the absorptive effects of acoustic liners in a developing turbulent pipe flow exiting to open air. The unsteady pressure field was found to experience an attenuation of up to 30 dB. No hydrodynamic instabilities were observed in their DNS since the porous boundary was not intentionally tuned to the turbulent energy-containing scales. The linear stability analysis by Rahbari & Scalo (2017) using a turbulent base flow was the first to show that the assigned finite wall impedance excites otherwise stable modes into temporally growing ones when the wall resistance value falls under a threshold. Sebastian, Marx & Fortuné (2019) later performed the same simulations of Scalo *et al.* (2015) at different subsonic Mach numbers and for a different range of resonating frequencies, showing that, as expected, the spanwise coherence of the instability gradually disappeared as the resonating frequency ω_{res} surpasses the frequency of the energy containing eddies.

For high-speed flow applications, there has been an increasing demand to analyse the effect of porous coatings on hypersonic laminar boundary layer flows. In flight conditions, the vehicle walls cool the overlying flow, resulting in a destabilization of the so-called second-mode waves responsible for transition to turbulence in high-speed laminar flows (Fedorov 2011). Both theoretical and experimental studies (Rasheed *et al.* 2002) have confirmed that ultrasonically absorbing coatings (UAC) are capable of absorbing such waves and delay the transition. The earlier theoretical (or numerical) results mainly involve linear stability analyses, in which impedance boundary conditions in the frequency domain are used. For example, Fedorov *et al.* (2003) performed both a theoretical and experimental study about the felt metal coating on a 7° half-angle sharp cone. Stability analyses were conducted with the help of impedance boundary condition (IBC) to model the effect of UAC. The theoretical analyses show qualitatively good agreement with

the experimental study. The work by Zhao *et al.* (2018) searched for an improvement in the model proposed by Fedorov *et al.* (2006), by considering the coupling effect among neighbouring cavities/pores. Although few in number, there have been efforts to apply TDIBC to flow simulations to model the effect of porous coatings over hypersonic vehicles. For instance, Sousa *et al.* (2019) applied the currently adopted TDIBC technique to simulate the effect of UAC in a Mach 7.5 cone flow, with a broadband impedance (Patel, Gupta & Scalo 2017) fitted to match benchtop acoustic absorption measurements of UAC samples. The simulations have demonstrated the ability of TDIBC to model UAC's acoustic absorption in hypersonic environments.

The applications of TDIBCs in high-speed flow focus on laminar flow control and, to the authors' knowledge, no previous work has addressed the effects of porous walls on hypersonic turbulence. It is the authors' interest to investigate how a wall with complex impedance will affect a supersonic or hypersonic turbulent flow field. The objective of this study is in fact not to investigate attenuation of sound in supersonic/hypersonic boundary layers. The goal is to inform possible flow control design efforts for hypersonic turbulence, similar to what is done in studies of transitional boundary layers. The manuscript is arranged as follows. Formulation of the problem is given in § 2. The numerical methods and set-up are provided in §§ 3 and 4. Results and analyses are provided in §§ 5 to 7. Section 8 gives the final conclusion.

2. Problem formulation

2.1. Flow set-up

In this paper, large-eddy simulations (LES) of compressible turbulent channel flow over complex wall impedance are carried out, in which the upper wall is kept impermeable while the bottom wall allows for a finite permeability as sketched in figure 1. The coordinate set $(x, y, z) = (x_1, x_2, x_3)$ represents the streamwise, wall-normal and spanwise directions, respectively. Reference quantities are δ , a_w and T_w – the channel half-width, speed of sound and temperature at the wall. In addition, we denote $\langle \cdot \rangle_V$ as the volume-averaged value in the whole computational domain, yielding the definition of bulk density

$$\rho_b = \langle \rho \rangle_V. \quad (2.1)$$

Unless otherwise stated, δ , ρ_b , a_w , T_w are used for non-dimensionalization. The bulk Reynolds number is defined as

$$Re_b = \frac{\rho_b U_b \delta}{\mu_{ref}}, \quad (2.2)$$

where U_b is the bulk velocity defined as $U_b = \langle \rho u_1 \rangle_V / \rho_b$ and μ_{ref} is the reference dynamic viscosity, taken at the wall surface. Following the aforementioned reference values, the following relations are established between the acoustic Reynolds number Re_a and bulk Reynolds number Re_b

$$Re_a = \frac{\rho_b a_w \delta}{\mu_{ref}}, \quad M_b = \frac{U_b}{a_w}, \quad Re_b = Re_a M_b. \quad (2.3a-c)$$

In the current work, the bulk Mach number M_b is chosen as 1.50, 3.50 and 6.00, set by constant mass flux simulations. A different bulk Reynolds number, Re_b , has been carefully assigned for each given bulk Mach number so that all cases share a similar friction

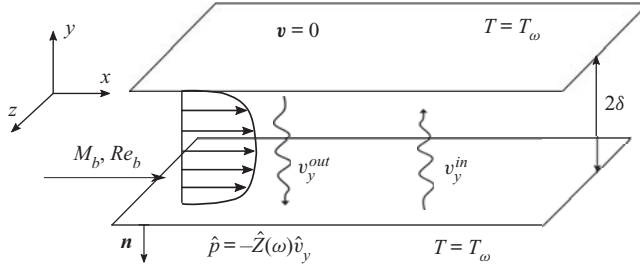


Figure 1. Flow set-up for turbulent channel flow over one permeable wall. The negative sign in the impedance boundary condition comes from the convention adopted in (1.1) regarding the direction of the surface normal, which in this case is opposite to the y axis.

Reynolds number $Re_\tau^* \approx 220$; the latter is a friction Reynolds number that accounts for variable density effects (Huang, Coleman & Bradshaw 1995) and is defined as

$$Re_\tau^* = \frac{\rho_c u_{\tau,c}^* \delta}{\mu_c}, \quad u_{\tau,c}^* = \sqrt{\tau_w / \rho_c}, \quad (2.4a,b)$$

where ρ_c , $u_{\tau,c}^*$ and μ_c are the density, shear velocity and dynamic viscosity at the channel centreline. As shown later in § 5, this approach allows us to keep the characteristic length scales of the turbulent buffer layer relatively constant across the three Mach number cases.

2.2. Governing equations

The simulations are performed by solving the compressible Navier–Stokes equations given as

$$\frac{\partial \rho}{\partial t} + \frac{\partial \rho u_j}{\partial x_j} = 0 \quad (2.5)$$

$$\frac{\partial \rho u_i}{\partial t} + \frac{\partial \rho u_i u_j}{\partial x_j} = -\frac{\partial p}{\partial x_i} + \frac{\partial \tau_{ij}}{\partial x_j} + \rho f_i \quad (2.6)$$

$$\frac{\partial \rho E}{\partial t} + \frac{\partial \rho u_j E}{\partial x_j} = -\frac{\partial p u_j}{\partial x_j} + \frac{\partial (u_k \tau_{kj} - q_j)}{\partial x_j} + \rho f_j u_j. \quad (2.7)$$

Here, τ_{ij} is the stress tensor given as

$$\tau_{ij} = (\mu + \mu_{sgs}) \left(\frac{\partial u_i}{\partial x_j} + \frac{\partial u_j}{\partial x_i} - \frac{2}{3} \delta_{ij} \frac{u_k}{x_k} \right), \quad (2.8)$$

with subscript ‘sgs’ being the component contributed by the sub-grid-scale model. The heat flux vector q_j is defined as

$$q_j = -C_p \left(\frac{\mu}{Pr} + \frac{\mu_{sgs}}{Pr_{sgs}} \right) \frac{\partial T}{\partial x_j}, \quad (2.9)$$

where C_p is the heat capacity at constant pressure, $\gamma = 1.4$ is the ratio of specific heats and $Pr = 0.72$ is the Prandtl number. The turbulent Prandtl number is chosen to be 0.9. For the constitutive relation, the ideal gas law $p = \rho R_{gas} T$ is used, where R_{gas} is the gas constant. A power law given by $\mu / \mu_{ref} = (T / T_{ref})^n$ is assumed for dynamic viscosity

with $n = 0.76$. The eddy-viscosity model by Vreman (2004) is used for turbulence closure, given as

$$\mu_{sgs} = \rho C_{Vr} \sqrt{(\beta_{11}\beta_{22} - \beta_{12}^2 + \beta_{11}\beta_{33} - \beta_{13}^2 + \beta_{22}\beta_{33} - \beta_{23}^2)/\alpha_{ij}\alpha_{ij}}, \quad (2.10)$$

where

$$\alpha_{ij} = \frac{\partial u_j}{\partial x_i}, \quad \beta_{ij} = \Delta_m^2 \alpha_{mi} \alpha_{mj}. \quad (2.11a,b)$$

Note that C_{Vr} is the model constant selected to be 0.07 and Δ_i is the grid spacing in the i th direction. To maintain the bulk mass flow rate and zero mean density and pressure gradient in the streamwise direction, a uniform body force is added to the streamwise momentum equation so that $\mathbf{f} = (f_1, 0, 0)$. The average value of f_1 is

$$\bar{f}_1 = \frac{\bar{\tau}_w}{\delta \rho_b}, \quad (2.12)$$

where $\bar{\cdot}$ represents the averaging operation and τ_w is the wall-shear stress. Periodic boundary conditions are used for the streamwise and spanwise directions. Wall boundary conditions are given as

$$u_1 = u_3 = 0 \quad (2.13a)$$

$$\begin{cases} u_2 = 0, & \text{impermeable.} \\ \hat{p} = -\hat{Z}(\omega)\hat{v}, & \text{permeable.} \end{cases} \quad (2.13b)$$

$$T = 1. \quad (2.13c)$$

Note that no-slip conditions are used for tangential velocity components due to the typical small pore size of porous walls/coatings used in high-speed flow applications; a commonly adopted assumption is, in fact, negligible tangential admittance for high-speed flows over porous walls (Fedorov *et al.* 2003; Sousa *et al.* 2019). The complex IBCs used in this work are different from Darcy-type porous boundary conditions, which model the finite-depth porous layer, also referred to as the 'sealed porous layer', typically dealing with a large pore size with respect to the boundary layer thickness, needing to account for all velocity components at flow–material interface. Inside the sealed porous layer, a separated equation, typically the Stokes equation (Abderrahaman-Elena & García-Mayoral 2017; Rosti, Brandt & Pinelli 2018) is solved; the current approach based on TDIBC incorporates the acoustic response within the pores into a boundary condition that only involves wall-normal velocity fluctuations and avoids directly resolving the pore geometry. For impermeable-wall calculations, the no-penetration condition is adopted for v , while for the permeable-wall simulations, a finite wall impedance $\hat{Z}(\omega)$ is prescribed. The negative sign in the impedance boundary condition arises from the convention of the surface normal used in (1.1).

3. Time-domain impedance boundary conditions

3.1. ADE method based on multi-oscillator wall softness

In this sub-section, the implementation of the TDIBC based on the ADE method is explained, which is built upon methodologies proposed by Dragna *et al.* (2015) and Troian *et al.* (2017). All TDIBC formulations involving the dependency on angular frequency

ω assume time harmonic behaviour $e^{i\omega t}$. To begin with, the pressure and surface-normal velocity at the bottom wall are replaced by domain-leaving and domain-entering waves, defined as

$$v_n^{out} = v_n - p'/\rho_s a_s, \quad v_n^{in} = v_n + p'/\rho_s a_s. \quad (3.1a,b)$$

Then, the impedance boundary condition can then be written as

$$\hat{v}_n^{in}(\omega) = [\hat{S}(\omega) - 1]\hat{v}_n^{out}(\omega), \quad (3.2)$$

with a time-domain correspondence

$$v_n^{in}(t) = -v_n^{out}(t) + \int_{-\infty}^{\infty} s(\tau) v_n^{out}(t - \tau) d\tau. \quad (3.3)$$

Here, $\hat{S}(\omega)$ is defined as the complex wall softness in the work by Fung & Ju (2004) as (see also Fung *et al.* (2000) and Fung & Ju (2001) for more details), and relates to the complex reflection coefficient $\hat{R}(\omega)$ via

$$\hat{S}(\omega) = \hat{R}(\omega) + 1 = \frac{2}{1 + \hat{Z}(\omega)}. \quad (3.4)$$

Both quantities $\hat{R}(\omega)$ and $\hat{S}(\omega)$ are measures of the phase and amplitude changes between incident and reflected waves. Values of 0, 1, 2 taken by $\hat{S}(\omega)$ represent surfaces of hard reflection, no reflection and pressure release, respectively. As stated, a robust and causal TDIBC can be constructed by designing an $s(t)$ that is zero on the interval $t \in (-\infty, 0)$. To achieve this, $\hat{S}(\omega)$ is first recast into the form of summations of rational functions as proposed by Lin *et al.* (2016)

$$\hat{S}(\omega) = \sum_{k=1}^{n_0} \left(\frac{\mu_k}{i\omega - p_k} + \frac{\mu_k^*}{i\omega - p_k^*} \right), \quad (3.5)$$

where the residues $\mu_k = a_k + ib_k$ and poles $p_k = c_k + id_k$ (here, the symbol p_k is used to represent poles, following the convention used by Lin *et al.* (2016), while in papers by Fung & Ju (2004) and Scalo *et al.* (2015) λ_k was used). The superscript $*$ denotes the complex conjugate of a complex number. The paring of rational functions guarantees $s(t)$ is real. This form is sufficient to model any impedance by fitting of the experimental data. From an input/output perspective, the causality constraint requires that the output signal, be it interpreted as either pressure or surface-normal velocity, should not depend on future values of the other one. If the form of IBC in (1.1) is implemented in the time domain directly as is, then a two-way causality must be satisfied to ensure a meaningful time-domain equivalence. This requires $\hat{Z}(\omega)$ to be analytic and free of zeros in the lower half of the ω -plane. In addition, $\int \hat{Z}(\omega) e^{i\omega t} d\omega$ must be integrable at complex infinity (Rienstra 2006). However, adopting the characteristic approach in (3.2) one can argue that only one-way causality is required between the characteristic waves impinging on the impedance boundary, v_n^{out} , and the resulting waves reflected off the boundary, v_n^{in} , re-entering the domain. From this perspective, current values of v_n^{in} should not depend on future values of v_n^{out} . With the form using the sum of rational functions proposed in (3.5), the causality constraint requires all the poles of $\hat{S}(\omega)$ (or zeros of $\hat{Z}(\omega) + 1$) to lie in the

upper half of the ω -plane, or in the left half of the Laplace domain (s -plane) with $s = i\omega$. The poles in (3.5) should therefore simply satisfy the condition

$$\operatorname{Re}(p_k) < 0, \quad (3.6)$$

which is equivalent to having all zeros of $1 + \hat{Z}(\omega)$ having a positive imaginary part on the ω -plane. It should be noted that $\hat{S}(\omega)$ being causal does not necessarily imply that $\hat{Z}(\omega)$ or $\hat{Z}^{-1}(\omega)$ is also causal. With the causality constraint, the expression of $s(t)$ can be obtained by taking the inverse transform of (3.5) and yields

$$s(t) = \sum_{k=1}^{n_0} (\mu_k e^{p_k t} + \mu_k^* e^{p_k^* t}) H(t), \quad (3.7)$$

where $H(t)$ is the Heaviside function as a result of the inverse transform, and is a direct consequence of imposing the causality constraint in the Fourier domain. This expression can be further simplified into the form

$$s(t) = \sum_{k=1}^{n_0} [2a_k e^{c_k t} \cos(d_k t) - 2b_k e^{c_k t} \sin(d_k t)] H(t). \quad (3.8)$$

Due to the null contribution of $s(t)$ in $t \in (-\infty, 0)$, the lower limit of integration in (3.3) can be replaced with 0

$$v_n^{in}(t) = -v_n^{out}(t) + \int_0^\infty s(\tau) v_n^{out}(t - \tau) d\tau. \quad (3.9)$$

Then, we combine (3.8) and (3.3), to get

$$\begin{aligned} v_n^{in}(t) = & -v_n^{out}(t) + \sum_{k=1}^{n_0} \left(\int_0^t 2a_k e^{c_k \tau} \cos(d_k \tau) v_n^{out}(t - \tau) d\tau \right. \\ & \left. - \int_0^t 2b_k e^{c_k \tau} \sin(d_k \tau) v_n^{out}(t - \tau) d\tau \right). \end{aligned} \quad (3.10)$$

Now we define

$$\psi_k^{(1)}(t) = \int_0^t 2a_k e^{c_k \tau} \cos(d_k \tau) v_n^{out}(t - \tau) d\tau = \int_0^t 2a_k e^{c_k(t-\tau)} \cos(d_k(t-\tau)) v_n^{out}(\tau) d\tau \quad (3.11)$$

$$\psi_k^{(2)}(t) = \int_0^t 2b_k e^{c_k \tau} \sin(d_k \tau) v_n^{out}(t - \tau) d\tau = \int_0^t 2b_k e^{c_k(t-\tau)} \sin(d_k(t-\tau)) v_n^{out}(\tau) d\tau, \quad (3.12)$$

and take derivatives of $\psi_k^{(1)}(t)$ and $\psi_k^{(2)}(t)$ with respect to time t to obtain

$$\frac{d\psi_k^{(1)}(t)}{dt} = c_{k-1} \psi_k^{(1)}(t) - d_{k-1} \psi_k^{(2)}(t) + v_n^{out}(t), \quad (3.13)$$

$$\frac{d\psi_k^{(2)}(t)}{dt} = c_{k-1} \psi_k^{(2)}(t) + d_{k-1} \psi_k^{(1)}(t). \quad (3.14)$$

The above ODEs can be discretized and advanced in time with the same numerical scheme as the main solver. The domain-entering wave is then calculated by

$$v_n^{in}(t) = -v_n^{out}(t) + \sum_{k=1}^{n_0} 2[a_k \psi_k^{(1)}(t) - b_k \psi_k^{(2)}], \quad (3.15)$$

and the resulting boundary condition in primitive variables can be calculated from (3.1a,b). For all simulations performed in this paper, the TDIBC is implemented with the same semi-implicit scheme as the main flow solver. A validation case of TDIBC against the classical impedance tube problem is given in Appendix B.1.

3.2. Choice of impedance model parameters

The three-parameter impedance model representing a single-pole Helmholtz oscillator proposed by Tam & Auriault (1996) is used in the current work

$$\hat{Z}(\omega) = R + i(X_+ \omega - X_{-1} \omega^{-1}), \quad (3.16)$$

where $R, X_+ > 0, X_{-1} > 0$ are acoustic resistance, acoustic mass-like reactance and acoustic spring-like reactance, respectively. This model can be tuned to absorb wave energy with characteristic frequency ω_{res} by setting

$$\omega_{res} = \sqrt{\frac{X_{-1}}{X_+}} \quad (3.17)$$

analogous to tuning the resonant angular frequency a mass–spring–damper system. Recall the damping ratio ζ defined by

$$\zeta = \frac{1 + R}{2\omega_{res}X_{+1}}. \quad (3.18)$$

In this paper, we only consider an under-damped system, that is, $\zeta < 1$. The impedance model can then be recast into the following form:

$$\hat{Z}(\omega_n) = R + i \frac{R+1}{2\zeta} \left[\omega_n - \omega_n^{-1} \right], \quad \text{where } \omega_n = \omega/\omega_{res}. \quad (3.19)$$

Hence, instead of using R, X_{-1} and X_{+1} as free parameters, the alternative set of R, ζ and ω_{res} can now be used. The corresponding complex wall softness is then

$$\hat{S}(\omega_n) = \frac{4\zeta(R+1)^{-1}\omega_n}{2\zeta\omega_n + i(\omega_n^2 - 1)}, \quad (3.20)$$

which can be shown to satisfy the reality constraint. The passivity constraint, directly assigned to $\hat{Z}(\omega)$, requires

$$R \geq 0. \quad (3.21)$$

The poles of the complex wall softness are given as

$$p_k/\omega_{res} = -\zeta \pm i\sqrt{1 - \zeta^2}, \quad (3.22)$$

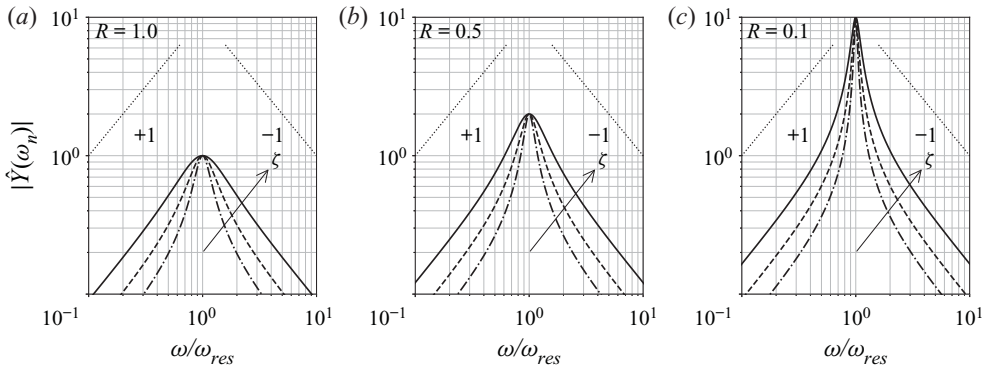


Figure 2. Magnitude of admittance vs dimensionless angular frequency for $R = 1.00$ (a), $R = 0.50$ (b) and $R = 0.10$ (c) with $\zeta = 0.3, 0.5, 0.9$.

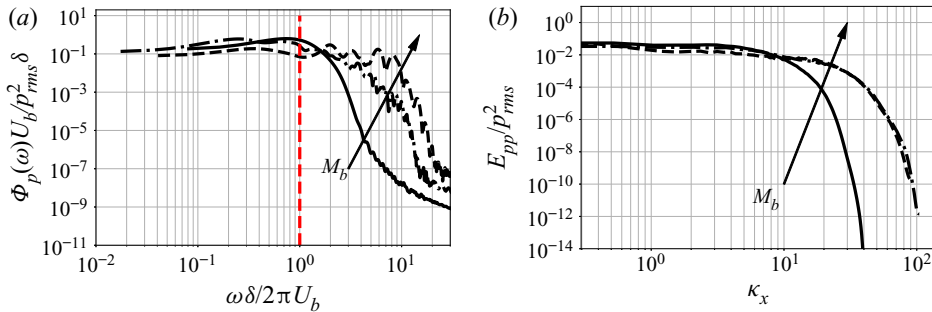


Figure 3. Scaled point-wise temporal spectra of wall pressure of impermeable channel flow (a) and wavenumber wall pressure spectrum (b). The vertical red dashed line denotes the location of the resonating frequency selected in (3.25). Data are obtained from the LES simulations discussed in § 5.

and the causality requires $\text{Re}(p_k) > 0$, thus

$$\text{Re}\{p_k\} = -\zeta < 0 \implies \zeta > 0. \quad (3.23)$$

Together with the under-damped assumption, one would get $\zeta \in (0, 1)$. The effect of varying ζ within the suggested range is shown in figure 2, which is not the main interest of this paper. For all permeable-wall simulations, ζ is set to 0.5, reducing the free parameters of IBC to two: R and ω_{res} . The quantity $\hat{Y}(\omega_n)$ is called the admittance, which is the inverse of the impedance $\hat{Z}(\omega_n)$, i.e.

$$\hat{Y}(\omega_n) = \hat{Z}^{-1}(\omega_n), \quad (3.24)$$

whose magnitude represents the wall permeability at the frequency ω_n . At resonating frequency, the magnitude of admittance achieves its maximum, with a value equal to R^{-1} , i.e. $\hat{Y}(1) = R^{-1}$. Preliminary tests have shown that a low resistance R will result in strong responses of the near-wall flow, leading to stringent constraints on the allowed Courant–Friedrichs–Lewy (CFL) number, especially at high Mach numbers. As a result, only resistance values beyond 0.10 are considered. Specifically, for $M_b = 6.00$, $R \geq 0.80$ is picked due to the unaffordable computational cost with low resistance.

The resonating angular frequency ω_{res} of the chosen IBC is the frequency at which the impedance wall is expected to yield the strongest reaction, and is set to be the characteristic

frequency of the energy-containing eddy in the flow, that is

$$\omega_{res} = 2\pi U_b/\delta. \quad (3.25)$$

This is verified in [figure 3](#), showing a typical temporal and spatial spectrum of the wall pressure. It can be seen that the choice in (3.25) provides a good approximation of where the most energetic frequency is located in the spectra.

4. High-fidelity Navier–Stokes solver

The compressible Navier–Stokes equations are solved by using the sixth-order compact finite differencing code CFDSU originally written by Nagarajan, Lele & Ferziger (2003), and under continuous development at Purdue for applications to various types of flow problems such as LES modelling (Chapelier, Wasistho & Scalò 2018), vortex dynamics (Chapelier, Wasistho & Scalò 2019) and hypersonic transitional flow (Sousa *et al.* 2019). The solver utilizes a staggered grid arrangement. All thermodynamic variables including density ρ , pressure p and temperature T are stored at cell centre while the velocity components and their associated conservative variables are stored at cell faces. Grid transformation is applied to enable simulations on curvilinear grids. In the current flow set-up, finite wall impedance will lead to a strong response near the wall and thus reduces the maximum allowable time step. To alleviate the constraint, a semi-implicit time advancement scheme is developed to stabilize the simulation, especially at higher Mach numbers. The scheme is a combination of a fully implicit scheme (Beam & Warming 1976, 1978; Pulliam & Chaussee 1981; Nagarajan *et al.* 2003) and the explicit Runge–Kutta scheme used by Akselvoll & Moin (1995). In such a scheme, the flux with the most stringent CFL constraint (mainly the wall-normal derivative terms) is treated implicitly and linearized in time to achieve a second-order temporal accuracy. The approximation factorization allows the resulting matrix-inversion problem to be solved iteratively with relatively low cost by using alternating direction implicit sweeping. This scheme is used for all cases presented in the current work.

5. Compressible turbulent channel flow over impermeable walls

To provide baseline cases for permeable-wall simulations, flow over impermeable walls at various Mach numbers is first investigated. [Tables 1](#) and [2](#) provide a summary of the flow conditions and grid resolutions for all impermeable-wall simulations. The domain size for $M_b = 1.50$ and 3.50 is $L_x \times L_y \times L_z = 12\delta \times 2\delta \times 4\delta$. For $M_b = 6.00$, a longer streamwise box with dimensions $L_x \times L_y \times L_z = 16\delta \times 2\delta \times 4\delta$ is used since the intense wall cooling leads to an increase in the coherence of the near-wall structure, consistent with the findings of Duan, Beekman & Martin (2010). The two-point correlations of primitive variables are provided in [Appendix C](#) to assess the suitability of the current domain size. The dimensionless wall heat flux is defined as (Rotta 1960)

$$B_q = \frac{q_w}{\rho_w C_p u_\tau T_w}. \quad (5.1)$$

Grid spacings are reported in terms of wall units (with superscript ‘+’), normalized by the viscous length scale calculated at the wall $\ell_{vis} = \mu_w/(\sqrt{\rho_w \tau_w})$ and the star unit (with superscript ‘*’), normalized by the length scale calculated at channel centre $\ell_{vis}^* = \mu_c/(\sqrt{\rho_c \tau_w})$. Unless otherwise stated, all mean flow statistics are calculated via Favre averaging (Wilcox 1998) in time and over planes parallel to the walls. For a generic flow

M_b	Case	Re_b	$L_x \times L_y \times L_z$	$N_x \times N_y \times N_z$	T_w/T_{cl}	$-B_q$
1.5	LES	5000	$12\delta \times 2\delta \times 4\delta$	$160 \times 192 \times 120$	0.73	0.04
	DNS	5000	$12\delta \times 2\delta \times 4\delta$	$320 \times 240 \times 240$	0.70	0.04
3.5	LES	10 000	$12\delta \times 2\delta \times 4\delta$	$400 \times 256 \times 240$	0.33	0.16
	DNS	10 000	$12\delta \times 2\delta \times 4\delta$	$800 \times 300 \times 500$	0.29	0.15
6.0	LES	20 000	$16\delta \times 2\delta \times 4\delta$	$480 \times 300 \times 240$	0.14	0.30
	DNS	20 000	$16\delta \times 2\delta \times 4\delta$	$1000 \times 300 \times 600$	0.14	0.30

Table 1. Simulation parameters of impermeable-wall cases including the Mach number M_b , the bulk Reynolds number Re_b , the domain size and the number of grid points. Also included are ratio of wall temperature to centreline temperature and dimensionless wall heat transfer defined in (5.1). Values are the averaged result of top and bottom walls. All LES cases use Vreman's LES model with a model coefficient $C_{Vr} = 0.07$.

M_b	Case	Re_τ	Δx^+	Δy_{min}^+	Δz^+	Re_τ^*	Δx^*	Δy_{min}^*	Δz^*	$(h/\eta)_{max}$
1.5	LES	336.17	25.30	0.14	11.27	220.98	16.63	0.09	2.86	16.45
	DNS	354.54	13.34	0.12	5.93	220.32	8.29	0.07	1.76	8.78
3.5	LES	959.29	29.04	0.30	16.16	221.96	6.72	0.07	4.26	18.90
	DNS	1069.08	15.75	0.28	8.41	208.98	3.08	0.05	2.85	10.71
6.0	LES	2749.59	93.35	0.74	46.77	221.61	7.52	0.06	13.88	69.60
	DNS	2742.65	44.77	0.74	18.67	220.91	3.61	0.06	7.76	32.31

Table 2. Viscous Reynolds number Re_τ and grid resolution normalized with wall units $\mu/\rho u_\tau$. The subscript 'min' represents the minimal value across the whole channel, which appears at the first grid point away from the wall. Also included is the viscous Reynolds number that accounts for the variable density effect Re_τ^* (Huang *et al.* 1995). The grid spacings with superscript '*' are obtained by $\Delta x_i^* = \Delta x_i^+ Re_\tau^*/Re_\tau$. Also included is the maximum value of ratio of grid size to local Kolmogorov length scale.

variable ψ , its Favre-averaged mean value $\tilde{\psi}$ and the corresponding fluctuation ψ'' are defined as

$$\tilde{\psi} = \frac{\bar{\rho}\bar{\psi}}{\bar{\rho}}, \quad \psi'' = \psi - \tilde{\psi}. \quad (5.2a,b)$$

Because of the CFL constraint set by the non-zero wall-normal velocity, the allowable time step decreases for increasing wall permeability due to the strong response in vertical velocity v . This puts a constraint on the number of flow-through times that can be simulated, especially for low values of the resistance (i.e. high permeabilities). By comparing the statistics averaged with different time spacings and numbers of snapshots, 20 instantaneous three-dimensional snapshots equally spaced over 10 flow-through times have been considered enough to achieve acceptable statistics.

As previously mentioned, the bulk Reynolds number at each Mach number is picked to ensure approximately the same viscous Reynolds number $Re_\tau^* \approx 220$, which is confirmed in table 2. Figure 4 shows the contour plot of instantaneous streamwise velocity component u for all impermeable-wall LES at $y^* \approx 15$. Owing to the similar Re_τ^* , the streamwise streaks show a structural resemblance across the Mach number range being investigated, however, with a slight decrease in the spanwise size of the low-speed streaks as the Mach number increases. DNS with the same flow conditions are also performed to assess the accuracy of the LES cases; the resulting velocity contours are shown in figure 4(b,d,f). As expected, LES smooths the near-wall streak structure; this effect is more obvious in the spanwise than in streamwise direction. The Mach 6.00 DNS case is picked for

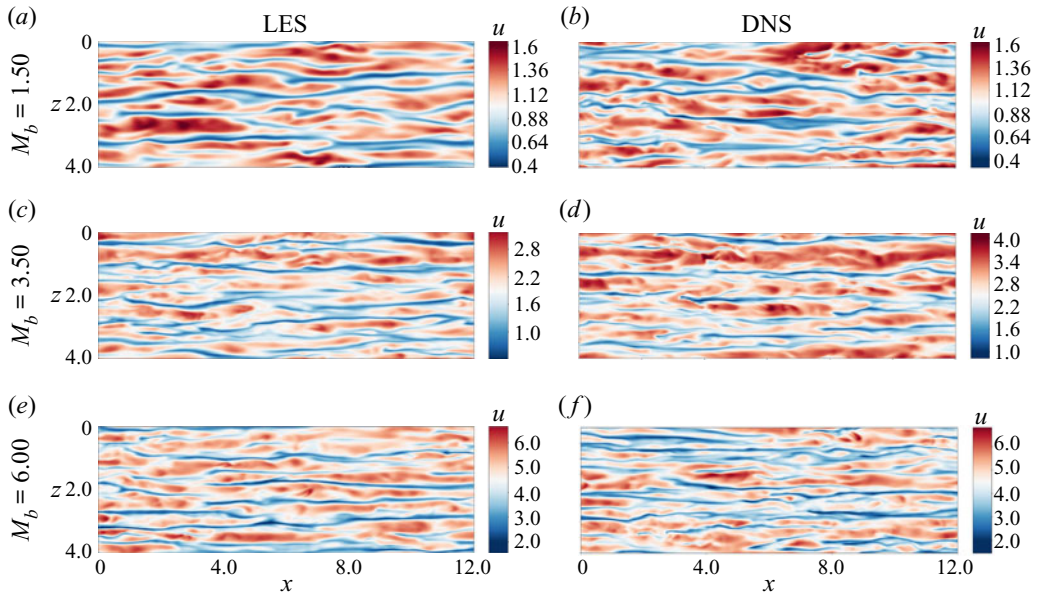


Figure 4. A comparison of the instantaneous streamwise velocity component at $y^* \approx 15$ for LES (a,c,e) and DNS (b,d,f). The y -axis is pointing towards the reader. For $M_b = 6.0$, the visualization domain size was cut to match the lower Mach number cases.

a grid convergence study due to its most stringent resolution requirement. The spatial velocity spectra in terms of streamwise and spanwise wavenumbers, κ_x and κ_z , are shown in [Appendix C](#), which indicates a more stringent resolution requirement in the streamwise directions. The resolutions based on the local Kolmogorov length scale are also given in [table 2](#). Quantities reported are the maximum ratio of averaged local grid size $h = (\Delta x \Delta y \Delta z)^{1/3}$ to the local Kolmogorov length scale, i.e. $(h/\eta)_{max}$. A ratio of $h/\eta < 2.1$ is suggested (Pope 2000) through the whole flow field for DNS study, which is a very stringent requirement. Since the impedance boundary conditions used in this work are designed to react to large-scale motions, we consider the LES resolutions to be sufficient to uncover the dynamics of flow over complex impedance walls.

[Figure 5\(a\)](#) shows the mean streamwise velocity U_{TL} , obtained with the transformation law by Trettel & Larsson (2016) and thus denoted with subscript ‘TL’. Such transformation has been shown to collapse mean velocity profiles onto the incompressible log law for channel flows at low and intermediate supersonic Mach numbers. For reference, compressible channel flow data by Ulerich (2014) ($M_b = 1.50$, $Re_b = 5000$) and the incompressible channel flow data from Lee & Moser (2015) with $Re_\tau \approx 180$ are also plotted. As observed in the baseline impermeable LES results, the mean velocity profile shows an overestimation of the intercept at $M_b = 1.50$; for high Mach numbers, the agreement between LES and DNS improves. [Figure 5\(b\)](#) to [figure 5\(d\)](#) present the resolved turbulent kinetic energy $k^* = \widetilde{u_i' u_i'}/2$ from the LES cases, along with the DNS data. Acceptable agreement is also achieved here, with the main discrepancy appearing in the peak of turbulence kinetic energy (TKE) around $y = 0.08$ in the $M_b = 1.50$ case. The overall agreement between the impermeable baseline LES and the corresponding DNS data validates the use of the impermeable LES presented herein as the base flow for the following stability analysis. From here on, only results from impermeable and permeable

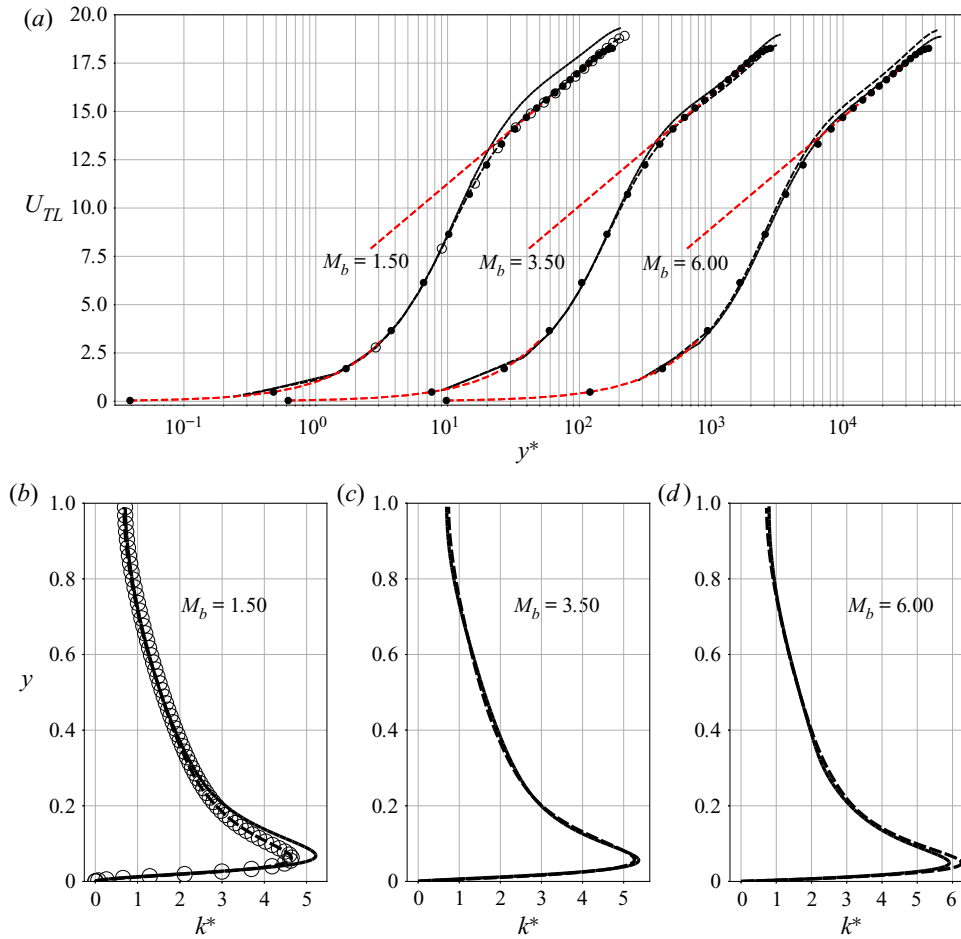


Figure 5. Flow statistics for impermeable channel flow simulations. Mean streamwise velocity profile (a) shifted horizontally by 1.2 decade (in log scale) and turbulent kinetic energy (b–d). Data shown are: current impermeable-wall LES (black solid line), DNS (black dashed line). DNS data from Ulerich (2014) (circles), incompressible flow data from Lee & Moser (2015) (black filled circles), shown every four points for clarity. The reference log law $U_{TL} = 2.5 \ln y^* + 5.5$ and law of the wall $U_{TL} = y^*$ are shown in red dashed lines.

LES calculations will be used to investigate the dynamics of compressible turbulence over complex impedance walls.

6. Compressible turbulent channel flow over complex impedance

In this section, the results of permeable-wall cases are presented. The bulk Reynolds number and the bulk Mach number are chosen to be the same as the impermeable baseline simulations. The domain size for all permeable-wall cases have been shortened $L_x \times L_y \times L_z = 8\delta \times 2\delta \times 4\delta$ for $M_b = 1.50$ and $M_b = 3.50$, and $L_x \times L_y \times L_z = 12\delta \times 2\delta \times 4\delta$ for $M_b = 6.00$, based on the observation that the streamwise coherence length is reduced by the wall permeability. The two-point correlations of primitive variables (not shown) confirm the validity of such a choice of domain size. Grid resolutions in wall units are

M_b	R	Bottom wall (porous)					Top wall				
		Δx^+	Δy_{min}^+	Δz^+	ΔU_{TL}	q_w	Δx^+	Δy_{min}^+	Δz^+	ΔU_{TL}	q_w
1.5	0.10	31.76	0.21	15.88	10.21	-0.02	21.88	0.15	10.94	N/A	-0.01
	0.50	22.87	0.15	11.44	3.27	-0.01	21.40	0.14	10.70	-1.87	-0.01
	1.00	21.53	0.14	10.77	0.90	-0.01	20.94	0.14	10.47	0.28	-0.01
3.5	0.50	24.05	0.27	13.63	1.84	-0.15	23.01	0.26	13.05	1.82	-0.14
	1.00	30.22	0.32	17.01	2.20	-0.15	29.38	0.31	16.53	0.81	-0.14
6.0	0.80	91.78	0.88	45.95	2.59	-0.60	94.00	0.90	47.07	-0.23	-0.62
	1.00	90.88	0.87	45.50	1.14	-0.59	94.02	0.90	47.07	-0.94	-0.62

Table 3. Grid resolutions in wall units for permeable-wall cases. Shifts in the intercept of the mean streamwise velocity profiles are reported in terms of ΔU_{TL} . Top wall and bottom wall data are reported separately.

listed in table 3. Validation of TDIBC implementation in such a flow is provided in Appendix B.

The mean streamwise velocity profiles scaled by bulk velocity are presented in figure 6(a) for permeable-wall cases. Profiles from impermeable-wall LES cases are also included as reference and shown with solid lines. Due to only the bottom wall being porous, the mean velocity profile exhibits an asymmetric pattern as compared with the impermeable-wall cases: the lower half of the channel shows a deficit in streamwise velocity while the upper channel exhibits an overshoot. The latter is merely due to the imposition of the same bulk velocity across all cases. Profiles over the bottom wall are plotted against semi-local unit y^* and are shown in figure 6(b). Downward shifts of the scaled mean velocity profiles in the log-law region are observed at various Mach numbers, similar to the effect observed in turbulent flows over rough surfaces. For rough walls, the shift usually indicates the increase of the mean wall-shear stress (Raupach, Antonia & Rajagopalan 1991; Squire *et al.* 2016), which is indeed observed in the current work. The shifts are reported in table 3 for all cases in terms of ΔU_{TL} , calculated as the averaged vertical shift between two curves in the range of $y^* = 60\text{--}100$. At $M_b = 1.50$, ΔU_{TL} increases as the permeability increases, i.e. as R is decreased, indicating a higher mean wall-shear stress. For higher Mach numbers, different resistances do not exhibit significant differences in the shift as in the low Mach number case. Note that, for $M_b = 1.50$, $R = 0.1$, a logarithmic trend for the upper mean velocity profile cannot be identified. The density-weighted root-mean-square (r.m.s.) wall-normal velocity fluctuations \tilde{v}_{rms}'' are shown in figure 7 in semi-log scale. For most of the cases, the effect of finite permeability (i.e. $R < \infty$) seems to be confined near the wall and below $y^* = 14$, in the buffer layer. This is not true for the high permeability case $R = 0.1$ at $M_b = 1.50$, in which \tilde{v}_{rms}'' sees an increase across the whole lower half-channel. In the latter case, the effects of the porous walls are globally felt by the boundary layer.

To better understand the increase in mean wall shear, the instantaneous value of τ_w is monitored at the bottom wall. Figure 8 presents the probability density function (PDF) of the instantaneous wall shear extracted from the bottom wall for all cases. Values are normalized with the mean wall-shear stress over an impermeable wall (i.e. $R = \infty$) to reflect the deviation from baseline cases. For every grid point on the bottom wall, sufficient data of the instantaneous wall-shear stress τ_w are recorded over the characteristic time period $-2\pi/\omega_{res}$ for permeable-wall cases and δ/U_b for impermeable-wall cases, which in total forms 491 520 data points for each case and guarantees the convergence of statistics.

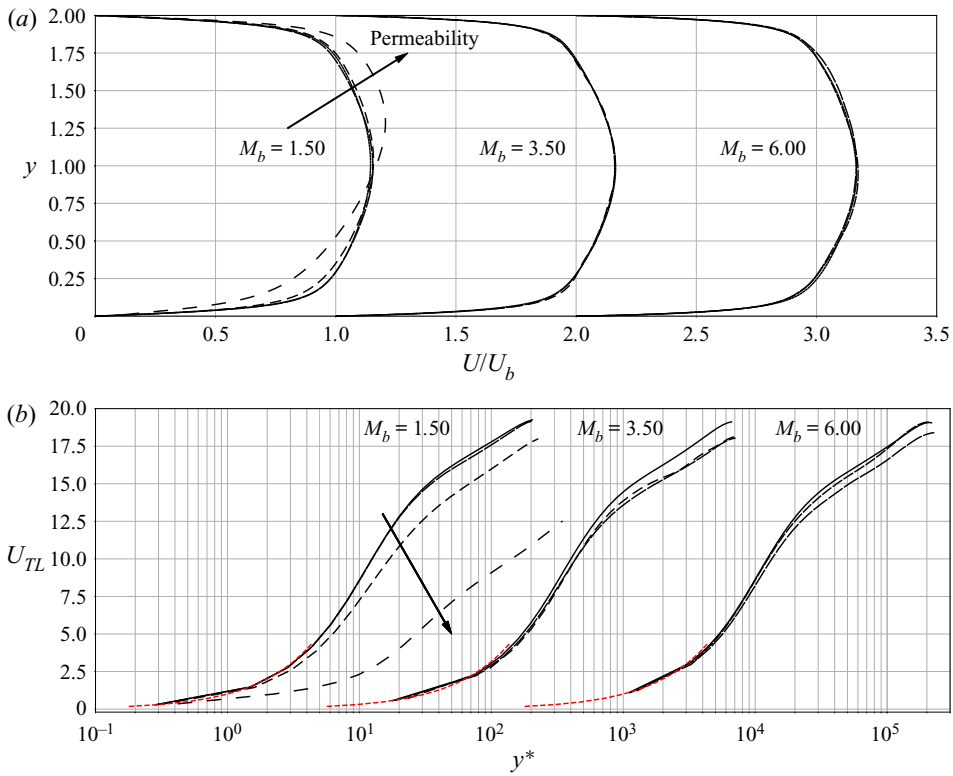


Figure 6. (a) Mean streamwise velocity profiles with various wall permeabilities normalized by bulk velocity U_b . (b) Mean streamwise velocity profiles based on TL-transformation in the lower half of the channel. Data shown are: $R = \infty$ (black solid line), $R = 1.00$ (black dashed dot line), $R = 0.80$ (only for $M_b = 6.00$) (black dashed line), $R = 0.50$ (black dashed line), $R = 0.10$ (black dotted line). Arrow shows direction of decreasing resistance R (increasing permeability).

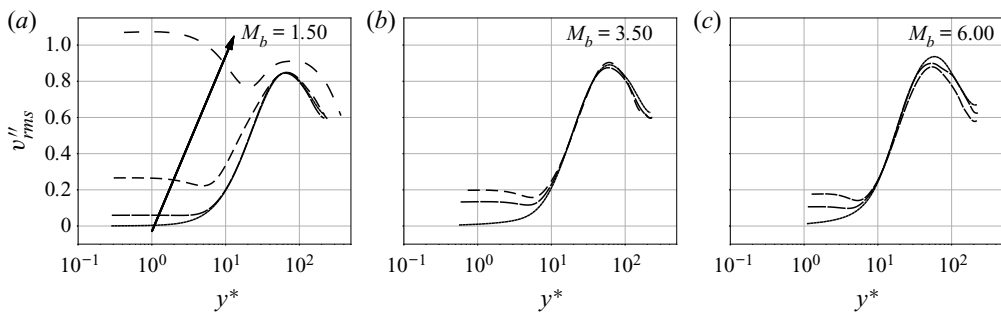


Figure 7. The root-mean-square (r.m.s.) wall-normal velocity fluctuations \bar{v}''_{rms} of permeable-wall cases, plotted against wall distance normalized by the semi-local unit. Arrow shows direction of decreasing resistance R (increasing permeability).

The impermeable wall results show a right-skewed PDF shape, with a peak located at the mean wall-shear stress. As the wall permeability increases, this peak shifts to the left and the PDF exhibits a longer right tail, indicating a drop in the value of the most frequently observed wall-shear stresses and an enhancement of extreme cases of positive shear stress.

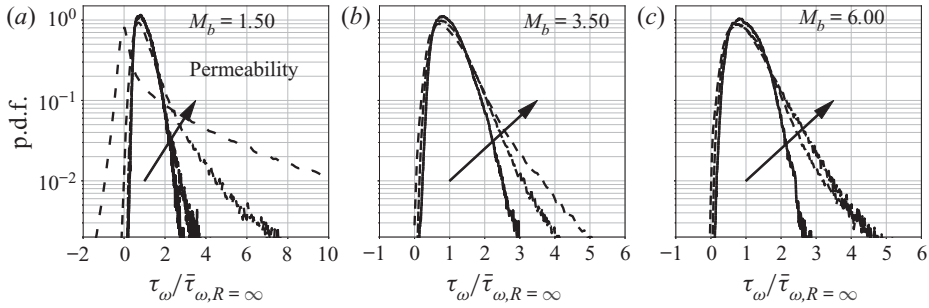


Figure 8. PDF of wall-shear stress at the bottom wall normalized by the impermeable-wall value for all LES cases listed in table 3. Arrows show direction of increasing permeability.

A closer examination the flow dynamics reveals the cause of such change in the instantaneous wall-shear stress, as shown in Figure 9(a), where the Q -criterion (Hunt, Wray & Moin 1988) is used to visualize the near-wall flow structures. The contour of instantaneous wall-shear stress is also plotted. Trains of streamwise-travelling waves triggered by porosity are observed beneath the otherwise naturally present near-wall streaks and hairpin vortices. Such instability waves entail spatially oscillatory wall-shear stress and pressure patterns in the streamwise direction, and spanwise oriented vortical regions captured by the Q -criterion (see figure 9a,b). A zoomed view, as given in figure 9(c), clearly shows the alternation of high and low pressure regions. The high pressure regions are found to be associated with flow entrainment – the suction effect due to the outgoing wall-normal velocity, while spanwise vortical structures are regions of circulation. The impingement of the fluid onto the wall surface induces cross-flow motion as a direct effect of the fluid being expelled to the spanwise direction. This behaviour is preserved at higher Mach number $M_b = 6.00$, although with weaker strength due to the relatively high resistance $R = 0.80$. The existence of these waves affects the near-wall turbulence dynamics. As an example, they contribute to the near-wall production of TKE. We define the spectrum of the production as

$$\hat{p}^k = -\frac{1}{2} \left[\left\langle \text{Re} \left\{ \widehat{\rho u' v'^*} \frac{d\tilde{u}}{dy} \right\} \right\rangle_{z,t} + \left\langle \text{Re} \left\{ \widehat{\rho v' u'^*} \frac{d\tilde{u}}{dy} \right\} \right\rangle_{z,t} \right], \quad (6.1)$$

where $\langle \cdot \rangle_{z,t}$ represents a averaging operator in the spanwise direction z and in time t . Then the pre-multiplied production spectrum given as

$$\hat{\Phi}_{\hat{p}^k, x} = Re_t^* \kappa_x y \hat{p}^k \mu / \tau_w^2 \quad (6.2)$$

can be plotted as a function of the streamwise wavelength λ_x (or wavenumber κ_x) and distance away from the wall y . The spectra $[\hat{\Phi}_{\hat{p}^k, x}]$, where the bracket indicates values normalized to one, are shown in figure 10 for the highest permeability available at each Mach number. For flows with finite wall permeability, a contribution from large wavelength structure is preserved, rendered as a horizontal band of hotspots in the region $\lambda_x > 1.0, y > 0.05$. For the case $M_b = 1.50, R = 0.10$, this band is less visible due to the normalization and the high peak value in another region. For each permeable-wall case, a local peak of the production spectrum appears in the very-near-wall region with an associated wavelength. This wavelength λ_x (scaled with the channel's half-width) is

Trapped waves in high-speed turbulent flow over porous walls

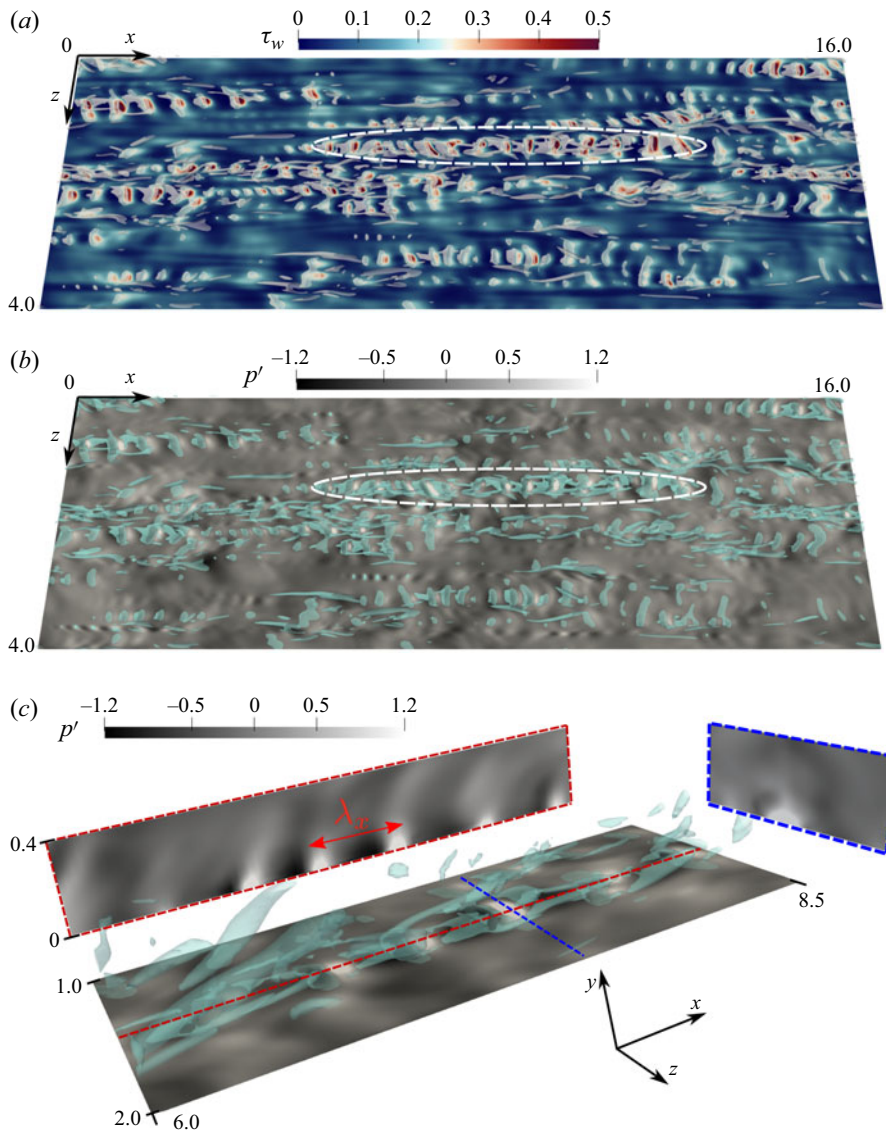


Figure 9. Visualizations of the near-wall flow dynamics for case $M_b = 6.0, R = 0.80$, presented with iso-surfaces of $Q = 90$ overlaid on: (a) instantaneous wall-shear stress contours; (b) wall pressure fluctuations. The region highlighted by the ellipse indicates a typical wave structure triggered by finite permeability, whose zoomed view is presented in (c), where red and blue dashed lines indicate locations of the plane presented in side views.

consistently equal to approximately 0.47 for all Mach numbers, and is found to match that of the observed wave structures in the simulations. Locations of local peaks above the wall do not experience discernible variations with different permeabilities, but gradually move closer to the wall as the Mach number increases, indicating a ‘trapped’ behaviour of such wave structure at high Mach numbers. In the equivalent subsonic calculations by Scalo *et al.* (2015), a strong hydrodynamic response was observed and it manifests itself with the presence of large spanwise-coherent rollers, which occupy a large portion of the boundary layer (approximately 20 % of the semi-channel height). In such subsonic calculations,

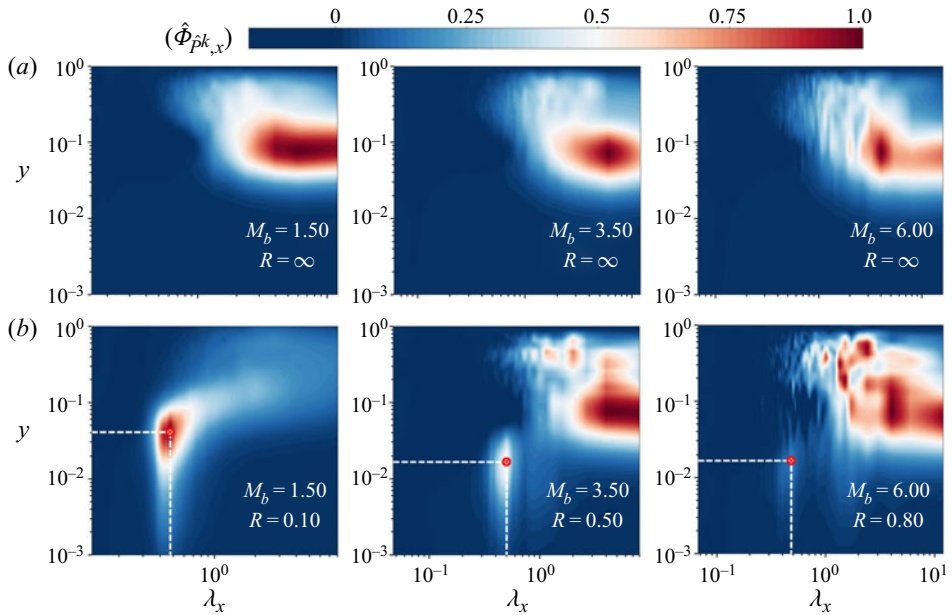


Figure 10. Contour plots of pre-multiplied production spectrum $\hat{\Phi}_{\hat{p}k,x}$ as a function of streamwise wavelength λ_x and distance away from the wall y . For each Mach number, the cases with an impermeable wall (first row) and with the highest wall permeability (second row) are presented. The location of the local peak due to finite permeability is labelled with a symbol.

a much lower value of the wall resistance, $R = 0.01$ was applicable to the flow, which is responsible for the strong response. As discussed in this manuscript, increasing the Mach number up to the hypersonic regime makes the adoption of resistances below $R = 0.8$ impossible due to numerical blow up. In the hard incompressible limit, such as in the work by Jiménez *et al.* (2001), such rollers are even larger, occupying the whole channel width. As the Mach number is increased past subsonic, and entering the supersonic and hypersonic regimes, the nature of the instability waves becomes more dilatational and more confined near the wall, typically below the turbulent buffer layer. The only exception is the $M_b = 1.5$ case for low resistance value $R = 0.1$, which resembles more the incompressible behaviour observed in Jiménez *et al.* (2001). A turbulent channel flow with isothermal wall features an increasing wall-cooling effect as M_b is increased. There is a possibility that such a phenomenon resembles the amplification of second-mode waves in cooled hypersonic boundary layers, in which an enhancement in wall cooling (or the wall-to-recovery temperature T_{wall}/T_r) yields a stronger instability in the hypersonic laminar boundary layer flow Fedorov (2011).

The impedance boundary condition defines the phase and amplitude relation between pressure and velocity signals at the wall. This concept could be extended to wavenumber space, in order to relate it to structural features of turbulence, in which one can also define an impedance $\hat{Z}(\kappa)$, or its inverse, admittance $\hat{Y}(\kappa)$, as

$$\hat{Y}(\kappa; y) = \bar{\rho}(y)\bar{a}(y)\hat{v}(\kappa; y)/\hat{p}(\kappa; y), \quad (6.3)$$

where κ can take on values of κ_x or κ_z denoting streamwise and spanwise wavenumbers, respectively. A plot of $||\hat{Y}(\kappa_x)||$ is shown in figure 11 for $M_b = 1.50$ with various permeabilities, at five y locations below a quarter of half-channel height, i.e. 0.25δ .

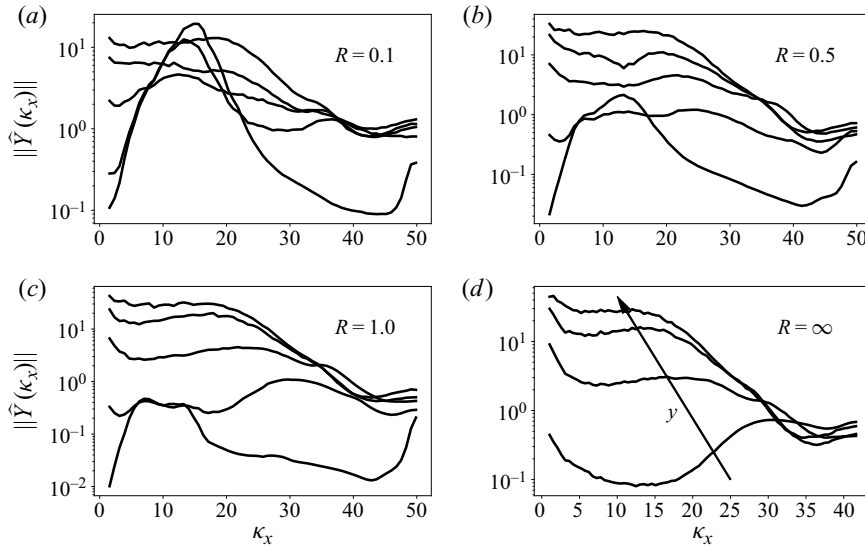


Figure 11. The magnitude of acoustic admittance as a function of streamwise wavenumber k_x for $M_b = 1.50$ with various wall permeabilities. Values of admittance are plotted at five y -location below a quarter of channel half-height. The impermeable-wall case has zero admittance on the wall due to the no-penetration condition and thus cannot be presented on a log-scale figure.

Note that the impermeable-wall case yields zero admittance on the wall because of the no-penetration condition, thus cannot be presented on a log-scale plot. Clearly, the effect of porosity-induced pressure/velocity phasing penetrates towards the channel centre for increasing wall permeability. The near-wall admittance peaks at the wavenumber corresponding to wave structures previously reported (the wavelength $\lambda_x = 0.47$). This then offers the opportunity to connect turbulence structure analysis and impedance boundary conditions. For typical turbulence structures residing in turbulent boundary layers or turbulent channel flows, their convective speed U_c and wavelength λ_x have obtainable scalings based on the semi-local unit for compressible flows (or the plus unit for incompressible flows). With this information, it would then be possible to construct a wall admittance $\hat{Y}(\omega)$ that resonates at $\omega_{res} = U_c \kappa_x$, where U_c and κ_x are the associated convective speed and wavenumber of the near-wall turbulent structure. In such a way, the boundary condition is then linked to the characteristic wavenumber (wavelength) of dominating structures in boundary layer type flows.

7. Linear stability analysis

In this section, temporal linear stability analysis (LSA) is performed at all flow conditions with various bottom wall permeabilities. To perform the analysis, the Navier–Stokes equations are linearized by decomposing each instantaneous variable into a base $\bar{\phi}$ and a fluctuation ϕ' component via

$$\phi = \bar{\phi} + \phi', \quad |\phi'| \ll |\bar{\phi}|. \quad (7.1a,b)$$

For channel flow, the base variable is independent of time while the small perturbation is assumed to have the harmonic form

$$\phi' = \hat{\phi}(y)e^{i(\alpha x - \Omega t)}, \quad (7.2)$$

where $i = \sqrt{-1}$; α and Ω are the streamwise wavenumber and angular frequency, respectively. Note that the symbol i also serves as the index in the Einstein notation, but only when it appears as a subscript. The angular frequency Ω is the opposite of ω as defined in the TDIBC formulation, favouring the convention used in wave propagation problems. The complex amplitude $\hat{\phi}$ is allowed to vary with distance away from the bottom wall. Polynomials at Gauss–Lobatto–Chebyshev points are used to approximate the solution and the problem is reformulated into a generalized eigenvalue problem (GEP) $\mathbf{A}\Phi = \Omega\mathbf{B}\Phi$, with the solution vector given by $\Phi = \{\hat{u}, \hat{v}, \hat{p}, \hat{T}\}^T$. The linearized governing equations are included in [Appendix D](#), along with code verification against results in the existing literature. Reynolds-averaged flow quantities from the impermeable-wall LES simulations in § 5 are used as the base flow profiles. To account for the background turbulent mixing, turbulent viscosity $\bar{\mu}_{turb}$ is added to the total viscosity in LSA, neglecting its perturbation μ'_{turb} . The turbulent viscosity can be obtained either by fitting an analytical model to a given flow condition, or by direct calculation via $\bar{\mu}_{turb} = \overline{\rho u''v''}/(dU/dy)$. For the first method, Cess (1958) has proposed an analytical form of μ_{turb} as a function of Reynolds number and pressure gradient in an incompressible turbulent pipe flow, which has been later adapted by Reynolds & Tiederman (1967) and Reynolds & Hussain (1972) for incompressible channel flow (see also Del Alamo & Jimenez 2006; Pujals *et al.* 2009; Rinaldi *et al.* 2017; Sebastian *et al.* 2019). The second method is more straightforward, but leads to error propagation due to the division operation. Nevertheless, for this study, the latter is used. Smoothing functions are applied near the channel centre where μ_{turb} is affected most by such an error. Then, the smoothed μ_{turb} is used in the mean streamwise momentum equation to re-obtain U through integration, which is compared to the Reynolds-averaged results from the simulations to ensure the validity of the calculated μ_{turb} .

The following boundary conditions are used in the LST study. No-slip and isothermal wall conditions lead to homogeneous Dirichlet boundary conditions for perturbations in temperature and streamwise velocity, that is, $\hat{u} = 0$ and $\hat{T} = 0$ at both walls. A non-homogeneous Neumann condition is used for pressure by applying the linearized wall-normal momentum equation (D7) at the wall grid point. Application of the impedance boundary condition with the adopted three-parameter model results in nonlinearity because of the Ω^{-1} dependence in the spring-like acoustic reactance term, and thus imposes difficulties in numerics. To circumvent this issue, the method suggested by Malik (1990) is used by introducing an auxiliary variable $\hat{\hat{v}} = \Omega\hat{v}$, extending the original solution vector to $\Phi = \{\hat{u}, \hat{v}, \hat{p}, \hat{T}, \hat{\hat{v}}\}^T$. The increase in computational cost is acceptable since only one more variable is added. Homogeneous Dirichlet condition is applied to \hat{v} for walls with zero permeability. For temporal linear stability problems, the wavenumber α is required as an input. Throughout this study, the wavenumber is fixed to $\alpha = 2\pi/\lambda_x$, with $\lambda_x = 0.47$, approximately matching the wavenumber of wave structures observed in the permeable-wall LES simulations. It has been pointed out by Hu & Zhong (1997) that spurious modes will appear in the GEP results when performing LST study, which can be easily identified via a grid convergence study since the locations of spurious modes in eigenspace are usually grid dependent. By using polynomial degrees in the range $N = 200, 300, 400, 500$ and comparing the eigenvalue spectrum, $N = 300$ is found to sufficiently resolve the spectrum in the region of interest for all Mach numbers. For all flow conditions, 20 values of $R = \{0.10, 0.20, \dots, 1.0, 2.0, \dots, 10.0, \infty\}$ are selected to conduct the study, where $R = \infty$ corresponds to the impermeable-wall case. [Figure 12](#) shows the spectrum of complex wave speed $c = \Omega/\alpha = c_r + ic_i$ scaled by bulk Mach number M_b . The trajectory

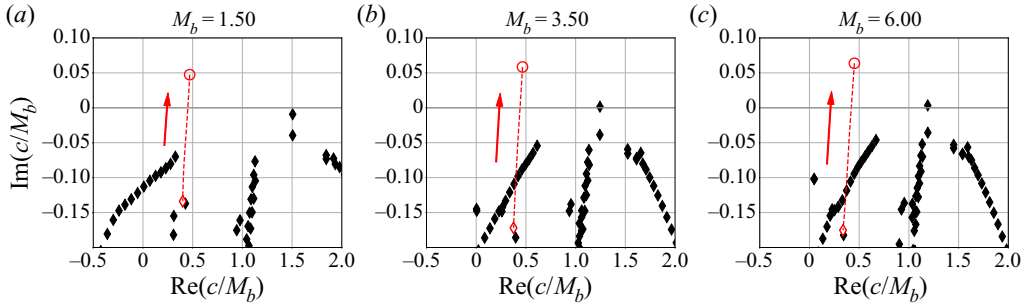


Figure 12. Eigenspectrum of a compressible turbulent channel flow for various bottom wall permeabilities for all bulk Mach numbers. The input wavenumber is taken as $\alpha = 2\pi/\lambda_x$ where $\lambda_x = 0.47$ is taken from the permeable-wall LES. The IBC resistance is varied in the range $R = \{0.10, 0.20, \dots, 1.0, 2.0, \dots, 10.0, \infty\}$. The red dashed line represents the trajectory of the mode affected by porosity with the arrow showing the direction of increasing permeability (or decreasing R). The filled black diamonds indicate scaled eigenvalues that do not vary with R , while red unfilled diamonds and circles represent the beginning ($R = \infty$) and the end ($R = 0.10$) of the trajectory of the mode affected by permeability, respectively.

of the mode affected by wall permeability is highlighted in red, while the black symbols represent modes in an impermeable-wall case, whose locations remain almost fixed when R varies.

Even with finite permeability, the overall spectrum retains the typical three-branch shape: a vertical stem roughly located at $\text{Re}\{c/M_b\} = 1$ indicating modes convecting at the bulk speed; two tilted branches that have zero or negative imaginary part, representing neutrally stable or damped modes. Introducing turbulent viscosity results in a strong damping effect on the modes belonging to left and right branches. A red dashed line highlights the trajectory of the mode made unstable by porosity, with a circle indicating the case with lowest resistance $R = 0.10$, i.e. highest wall permeability, and a diamond indicating the impermeable limit $R = \infty$. At any given Mach number, increasing the wall permeability (or decreasing R) increases the growth rate of this mode, gradually moving it towards the unstable region (upper half-plane). Figure 13(a) collects all trajectories of the permeability-triggered mode from different Mach numbers and wavenumbers. For unstable modes, higher Mach number favours a higher growth rate, but lower scaled phase velocity at a given resistance R . The points at which each trajectory crosses zero, defined as critical resistance R_{cr} , are extracted and shown in figure 13(b). A sub-linear dependence of R_{cr} on M_b is observed, which indicates that higher Mach numbers require low permeability to trigger such a type of instability.

It should be noted that for hypersonic bulk Mach numbers of $M_b = 6.0$ the linear stability predicts no unstable modes for values of resistance above ~ 0.77 ; however, a modal instability can still be detected in permeable-wall hypersonic LES calculations at $R = 0.8$. The latter is suppressed by increasing the resistance further to $R = 1.0$ indicating that the effective critical resistance value for hypersonic conditions is in the range $R_{cr} = 0.8$ – 1.0 . Such a range of critical values is still quite narrow compared with typical values of wall resistance observed in porous walls used for hypersonic applications, which can exceed $R = 10$ (Sousa *et al.* 2019) over a broad range of ultrasonic frequencies.

The angular frequency associated with the tracked mode can be obtained from the simple relation $\Omega_r = \alpha c_r$, where c_r is the real part of phase velocity. For values of R available in three-dimensional simulations, table 4 lists the scaled phase velocity c_r/M_b and normalized angular frequency Ω_r/Ω_{res} obtained from LST. A near-unitary value of Ω_r/Ω_{res} indicates that the frequency of the temporally growing mode is very close to the

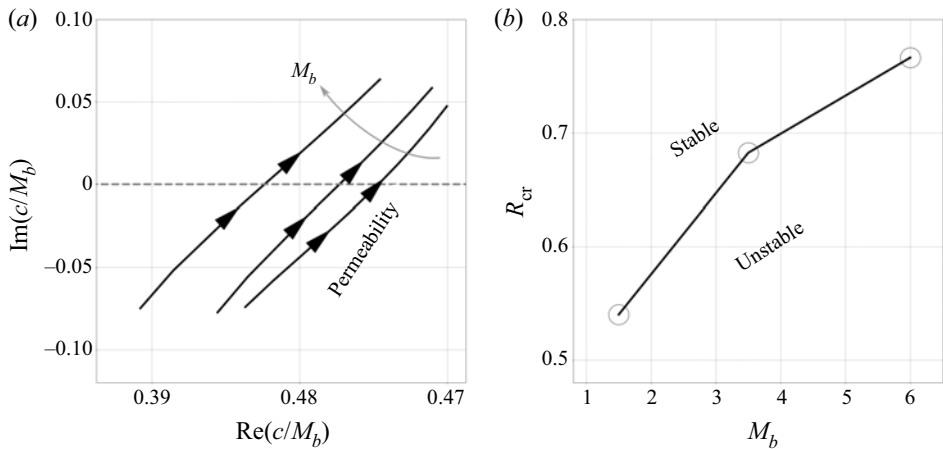


Figure 13. (a) Trajectory of an eigenmode tracked in red in figure 12 re-proposed here for all Mach numbers and a streamwise wavelength of $\lambda_x = 0.47$, as observed in the permeable-wall LES. Arrow shows the direction of increasing permeability (or decreasing R). (b) The critical resistance R_{cr} (unfilled circles) below which the mode in (a) becomes unstable as a function of bulk Mach number M_b .

M_b	R	$\text{Re}\{c/M_b\}$	$\text{Re}\{\Omega/\Omega_{res}\}$
1.5	0.10	0.469867858711176	0.999718848321527
	0.50	0.4526502643212107	0.963085668768534
	1.00	0.4382393119005271	0.932424067873462
3.5	0.50	0.4471177566617988	0.951314375876168
	1.00	0.4319650918846243	0.919074663584307
6.0	0.80	0.4193522754315207	0.892238883896853
	1.00	0.4135864384326250	0.879971145601330

Table 4. The scaled phase velocity and associated angular frequency of the tracked mode for values of resistance also investigated with LES. The angular frequency is normalized with the resonating frequency Ω_{res} .

resonating frequency of the IBC, at which the flow is excited the most. The eigenfunctions of \hat{p} and \hat{v} of the mode tracked in figure 12 are shown in figure 14. Only modes with $R < R_{cr}$ are shown. It is apparent that most of the perturbation energy is trapped in the near-wall region, consistent with the trapped wave pattern observed in the simulations as shown in figure 9. Figure 15 shows the contour plot of the pressure mode from LST prediction and the pressure fluctuation extracted from filtered LES results for the lowest resistance available at each Mach number. The latter contour plot was obtained by performing an average in the z -direction in a small box that contains the whole wave structure. A good resemblance is obtained in the pressure fluctuations between LST results and full-scale simulations. Top-down views of the contour plot of the pressure fluctuation on the wall are provided for the corresponding cases in figure 16. In fact two types of wave structures are observed at a fixed Mach number with different wall permeabilities, clearly with different wavelengths (it is difficult to observe these structures in the cases of $M_b = 1.50$). In the impermeable-wall simulations, these waves are associated with the ‘footprint’ of large streamwise scales and can still be observed in the permeable-wall

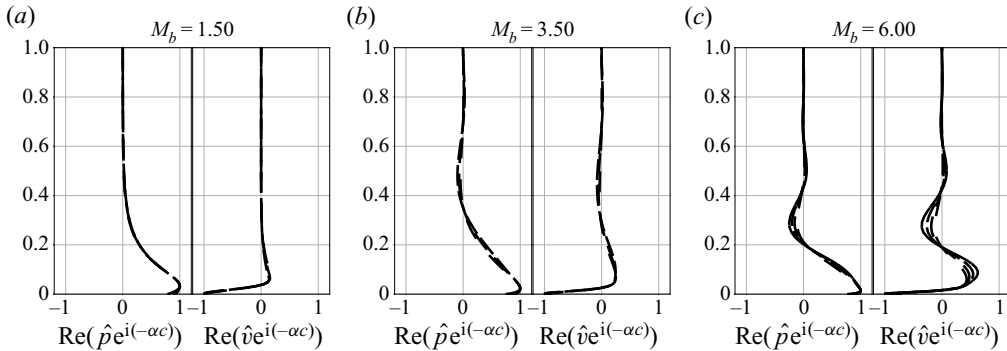


Figure 14. Scaled real part of the pressure and velocity eigenfunctions associated with the tracked mode for resistance values below R_{cr} at each Mach number. For clarity, only values of following R are selected to plot: $R = 0.10$ (black dotted line), $R = 0.30$ (black dotted line), $R = 0.50$ (black dotted line), $R = 0.70$ (black solid line).

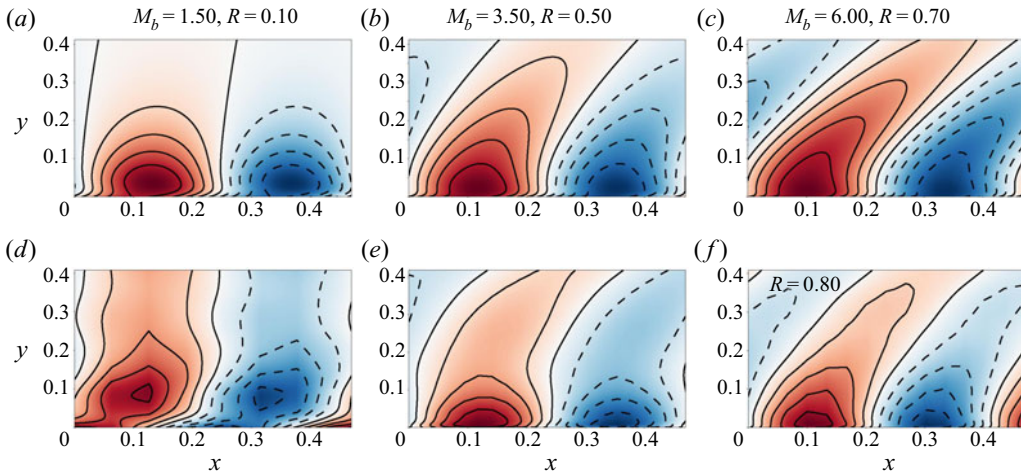


Figure 15. Contour of unstable pressure mode (a–c) from LST and pressure fluctuations near the wall extracted from the LES (d–f). Pressure fields from the three-dimensional simulations are first filtered with a bandpass Butterworth filter, keeping only the wavelengths in the range $[0.35, 0.5]$. A z -plane average is then performed on the filtered pressure field among planes that cut through the wave structures. Values are normalized with the maximum amplitude of pressure fluctuation. Positive and negative levels are shown with solid and dashed lines, respectively. Note that for the linear stability result at $M_b = 6.00$, the highest data point of R below R_{cr} is 0.70 instead of 0.80 used in the simulation.

simulations. With the finite wall impedance, these structures co-exist with waves with different length scale, triggered by the response of the permeable walls.

Although a good match is achieved between LST and simulations, one must keep in mind that temporal LST is meant to predict the stability of a linearly growing perturbation. In contrast, instability observed in the three-dimensional simulations has reached a saturation state due to the interaction between near-wall turbulence and acoustic response from the wall. Hence, the physical process that LST is predicting is the onset state of a complex IBC applied to the turbulent field developed over an impermeable wall.

The complex velocity field due to the instability is further decomposed into dilatational $\hat{\mathbf{v}}_d$ and solenoidal part $\hat{\mathbf{v}}_s$, i.e. $\hat{\mathbf{v}} = \hat{\mathbf{v}}_d + \hat{\mathbf{v}}_s$. To account for the contribution of the two

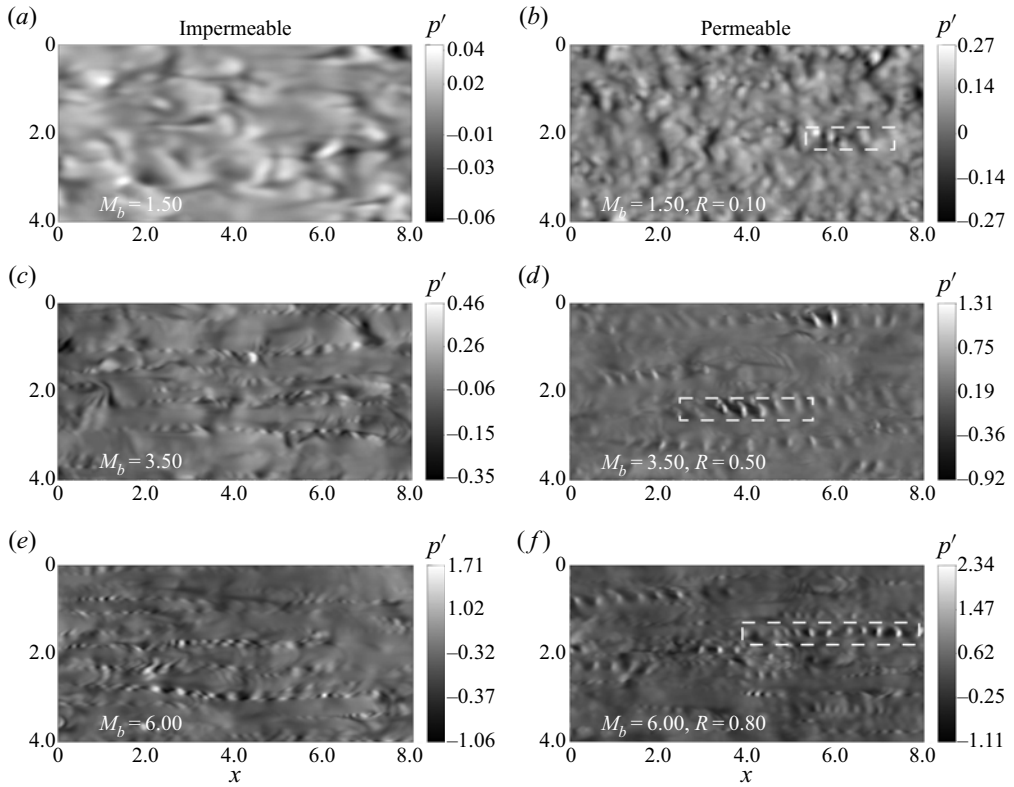


Figure 16. Top-down view of the pressure fluctuations on the bottom wall. Left column shows the LES impermeable-wall results, right column shows the permeable-wall cases presented in figure 15, with the white box showing the region where filtered pressure fields are extracted.

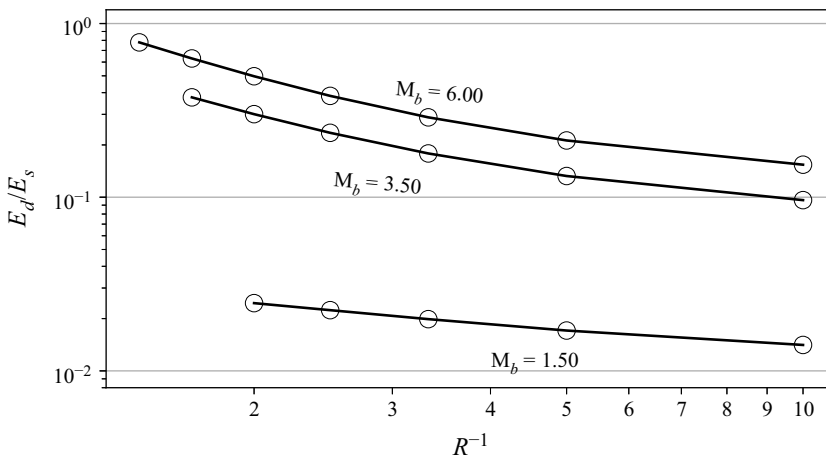


Figure 17. Ratio of the integrated norm of dilatational part \hat{v}_d and solenoidal part \hat{v}_s of the perturbed field, E_d/E_s , defined in (7.3) vs the inverse of the wall resistance. Results are obtained by applying the Helmholtz–Hodge decomposition to the velocity eigenfunctions of the unstable mode. Only resistance values below R_{cr} are shown here, with $\lambda_x = 0.47$.

components, the ratio of the integrated norm

$$\frac{E_d}{E_s} = \frac{\int_0^2 |\text{Re}\{\hat{v}_d e^{-\alpha c}\}|^2 dy}{\int_0^2 |\text{Re}\{\hat{v}_s e^{-\alpha c}\}|^2 dy} \quad (7.3)$$

is evaluated for the normal velocity component for cases with $R < R_{cr}$ for all Mach numbers. Results are shown in Figure 17 for wavenumbers (wavelengths) associated with those appearing in LES. At each Mach number, the dilatational field occupies a discernible amount of energy once the instability is triggered, and is gradually weakened as permeability increases. The perturbed flow fields exhibit a more hydrodynamic nature as the response of the impedance wall to the overlying turbulent field becomes stronger. In addition, the same (non-dimensionalized) permeability tends to yield a perturbed field with higher portion of dilatational energy at higher Mach number.

8. Conclusion

To examine the instability phenomenon of high-speed turbulent flows over porous media, LES of compressible turbulent channel flows over walls of various impedance have been performed at three bulk Mach numbers: $M_b = 1.50, 3.50$ and 6.00 . The bulk Reynolds number Re_b is tuned to achieve a similar viscous Reynolds number $Re_\tau^* \approx 220$ to ensure a resemblance of near-wall turbulence structures over impermeable walls. The TDIBC based on the ADE method is applied to the bottom wall of the channel. The three-parameter complex impedance model with a resonating frequency tuned to the large-eddy turn-over frequency of the flow is adopted.

Results show that a finite wall permeability has a significant effect on the near-wall turbulence. Increasing mean wall-shear stress has been observed when the permeability increases, as a statistical result of the more frequently appearing extreme instantaneous high wall-shear stresses compared with the impermeable-wall baseline case. At sufficiently low resistance, the visualization using the Q -criterion captured streamwise-travelling waves entailing high-low alternating wall pressure patterns. Such wave structures contribute to the production of TKE in the near-wall region at all Mach numbers, with the contribution weakening as the Mach number increases.

LSA using the turbulent background base flow confirms that the aforementioned instability is triggered by the finite wall permeability and is trapped near the bottom wall, when the resistance is below a threshold defined as critical resistance R_{cr} . The pressure mode shape extracted from LSA agrees well with those from the filtered LES simulations. The critical resistance R_{cr} is shown to be sub-linearly proportional to the bulk Mach number M_b , indicating that less permeability is required to trigger the instability in high Mach number flows. By applying Helmholtz decomposition of the perturbed velocity field obtained from LSA, it is shown that the occupation of the dilatational field gradually disappears as the response of the impedance wall to the overlying flow gets stronger, i.e. as R decreases.

For future work, it would be desirable to have experimental studies to confirm the behaviour and effect of the wave structures in high-speed flows. In addition, in the current study, the resonating frequency ω_{res} was picked to couple with the overlying turbulence, which is not necessary the case in real applications, neither are the resistance values

selected in this paper. Thus, future studies might also include parametric studies of ω_{res} and R , both of which can in fact have spatial variations.

Acknowledgements. The authors acknowledge the support of computational resources provided by the Rosen Center for Advanced Computing (RCAC) at Purdue University and the Extreme Science and Engineering Discovery Environment (XSEDE). C.S. acknowledges the support of the U.S. Air Force Research Laboratory (AFRL) DoD Supercomputing Resource Center (DSRC), via allocation under the subproject AFOSR43032009.

Funding. This work was supported by the National Science Foundation (NSF) Fluid Dynamics Program (Award No. 1706474) and the Air Force Research Office of Scientific Research (AFOSR) 2018 Young Investigator Award (YIP) (FA9550-18-1-0292).

Declaration of interests. The authors report no conflict of interest.

Author ORCIDs.

 Yongkai Chen <https://orcid.org/0000-0002-5243-8341>;

 Carlo Scalò <https://orcid.org/0000-0002-6774-2207>.

Appendix A. Semi-implicit time advancement scheme

In this section, some details of the semi-implicit time advancement scheme used in this work are presented. While this scheme is not novel *per se*, the authors have found that its adoption was necessary to stabilize calculations with strong flow responses such as the ones obtained for low resistance values $R < 0.5$ entailing strong wall-normal velocities near the boundaries. For simplicity, a shorthand notation of the governing equations is used here to illustrate the method

$$\mathbf{U}_t = \mathbf{A}(\mathbf{U}) + \mathbf{B}(\mathbf{U}), \quad (\text{A1})$$

where \mathbf{U} is the solution vector; $\mathbf{A}(\mathbf{U})$ and $\mathbf{B}(\mathbf{U})$ are explicit and implicit flux vectors, respectively. Then from time step n to $n + 1$, the k th stage of an explicit Runge–Kutta scheme can be written in the following form:

$$\left. \begin{aligned} \frac{\mathbf{U}^k - \mathbf{U}^{k-1}}{\Delta t} &= \beta_k [\mathbf{B}^k + \mathbf{B}^{k-1}] + \gamma_k \mathbf{A}^{k-1} + \zeta_k \mathbf{A}^{k-2}, \quad k = 1, 2, \dots, s \\ \mathbf{U}^0 &= \mathbf{U}^n, \quad \mathbf{U}^s = \mathbf{U}^{n+1} \end{aligned} \right\}, \quad (\text{A2})$$

where s represents the total number of stages of the explicit scheme, which is 3 in current method; α_k and β_k are coefficients given below

$$\left. \begin{aligned} \beta_1 &= 4/15 & \beta_2 &= 1/15 & \beta_3 &= 1/6 \\ \gamma_1 &= 8/15 & \gamma_2 &= 5/12 & \gamma_3 &= 3/4 \\ \zeta_1 &= 0 & \zeta_2 &= -17/60 & \zeta_3 &= -5/12. \end{aligned} \right\} \quad (\text{A3})$$

Then the problem is to approximate the flux \mathbf{B}^k , which is unknown at stage k . A linearization in time leads to

$$\left. \begin{aligned} \mathbf{B}^k &= \mathbf{B}^{k-1} + \left(\frac{\partial \mathbf{B}}{\partial \mathbf{U}} \right)^{k-1} \Delta \mathbf{U}^{k-1} + O(\Delta t^2), \\ \Delta \mathbf{U}^{k-1} &= \mathbf{U}^k - \mathbf{U}^{k-1} \end{aligned} \right\}. \quad (\text{A4})$$

To iteratively solve the system, sub-iterations can be incorporated into each stage to ensure

$$\lim_{l \rightarrow \infty} \mathbf{U}^l = \mathbf{U}^k. \quad (\text{A5})$$

The delta formulation is required here by replacing the terms at time level k with those at level l (not the coefficients)

$$\frac{U^l - U^{k-1}}{\Delta t} = \beta_k \{B^l + B^{k-1}\} + \gamma_k A^{k-1} + \zeta_k A^{k-2}. \quad (A6)$$

Linearizing B^l and rearranging (A6), one can arrive at

$$\left\{ I - \Delta t \beta_k \left(\frac{\partial B}{\partial U} \right)^{l-1} \right\} \Delta U^{l-1} = U^{k-1} - U^{l-1} + \Delta t \beta_k B^{l-1} + \Delta t (\beta_k B^{k-1} + \gamma_k A^{k-1} + \zeta_k A^{k-2}). \quad (A7)$$

The current implementation treats all wall-normal convective fluxes implicitly. For the viscous flux, only those containing second-order wall-normal derivatives are included. The detailed formulation, including the Jacobians, can be found in Nagarajan (2004). A test case will be shown in B.1 for validation.

Appendix B. Verification and validation of TDIBC implementation

B.1. Impedance tube test problem

A one-dimensional impedance tube problem is used to validate the implementation of TDIBC in CFDSU. A broadband wave pulse with initial shape is defined as follows on $y \in [0, 2]$ (at $t = 0$):

$$p'(y, t) = \frac{1}{2} A \exp(-\alpha k^2 (y - 1 - t)^2) \cos[2\pi k(y - 1 - t)], \quad (B1)$$

$$v'(y, t) = \pm p'(y, t), \quad (B2)$$

where ‘+’ and ‘−’ signs are used for initially up-travelling and down-travelling waves, respectively. With the assumption of linear advection of the waves, the solution is given by

$$v^\pm(y, t) = \frac{A}{4k} \sqrt{\frac{1}{\alpha\pi}} \int_{-\infty}^{+\infty} \frac{1 - \hat{Z}(\omega)}{1 + \hat{Z}(\omega)} \exp(\pm i\omega(y - t - 1)) \times \left[\exp\left(-\frac{(\omega/k + 2\pi)^2}{4\alpha}\right) + \exp\left(-\frac{(\omega/k - 2\pi)^2}{4\alpha}\right) \right] d\omega. \quad (B3)$$

The above integral is performed numerically for $t = 2.0$ at which the wave hits the wall once. The free parameters are selected to be $\alpha = 0.8$, $k = 7.0$, $A = 1e - 7$. This problem was tested by using ADE method with various spatial and temporal resolutions, with the spatial and temporal convergence study given in figure 18. Figure 19 presents the solution of an initially down-travelling wave, which agrees well with the numerically obtained analytical solution.

B.2. Validation of TDIBC applied to a turbulent channel flow

To check if the TDIBC has been correctly implemented in the simulation, the pressure–velocity cross-spectrum is examined, derived as

$$\hat{p}/\rho_w a_w = -\hat{Z}(\omega)\hat{v} \implies \hat{p}\hat{p}^*/\rho_w a_w = -\hat{Z}(\omega)\hat{v}\hat{p}^*. \quad (B4)$$

The phase and magnitude of $\hat{p}\hat{p}^*/\rho_w a_w$ and $-\hat{Z}(\omega)\hat{v}\hat{p}^*$ are compared in figure 20 for cases at $M_b = 1.50$. Good agreements are achieved in the magnitude of the spectrum.

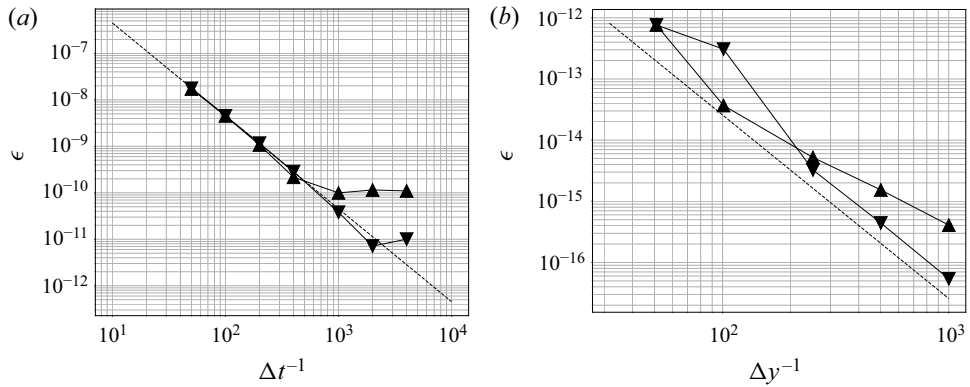


Figure 18. The spatial and temporal convergence study for the impedance tube test problem with initially up-travelling (\blacktriangle) and down-travelling (\blacktriangledown) waves. The dashed line represents a second-order convergence in (a) and a third-order convergence in (b). For the spatial convergence study, all cases are run with $CFL \approx 0.005$. For the temporal convergence study, 1001 grid points are used in the y direction.

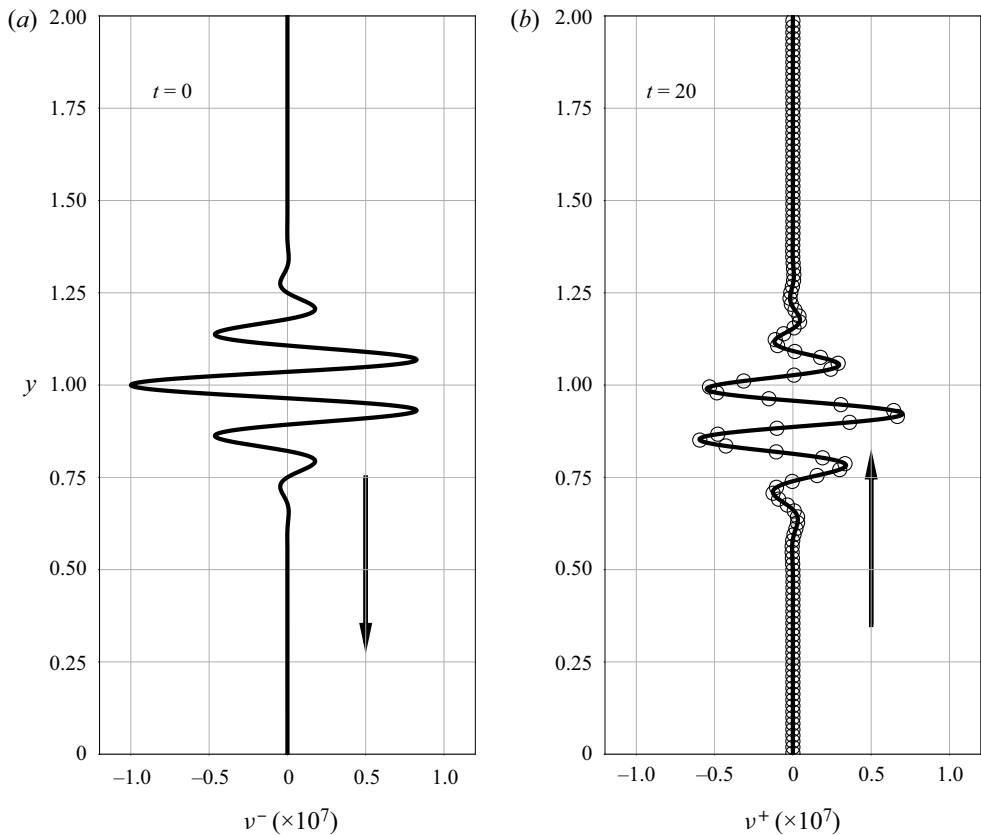


Figure 19. The impedance tube test case with an initially down-travelling broadband wave pulse. TDIBC is applied at the bottom wall. Initial condition at $t = 0$ (a) and result at $t = 2$ (b). Analytical solution at $t = 2$ (unfilled circles) is also shown (plotted every four points).

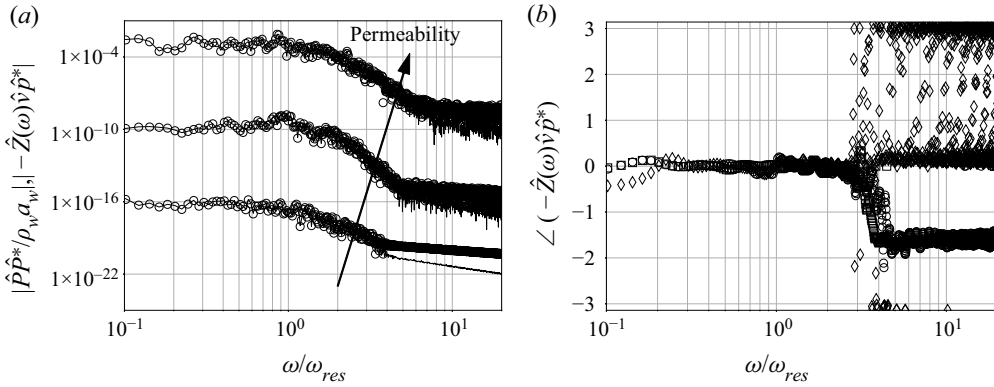


Figure 20. Magnitude (a) of the pressure-velocity cross-spectrum $\hat{v}\hat{p}^*$ for permeable-wall cases at $M_b = 1.50$. Magnitude of the data is shifted for clarity with the arrow showing the direction of increasing permeability (decreasing R). Quantities presented are $|\hat{p}\hat{p}^*/\rho_w a_w|$ (unfilled circles) and $|\hat{Z}(\omega)\hat{v}\hat{p}^*|$ (black solid line), which should match if the TDIBC is correctly implemented. The phase (b) of $|\hat{Z}(\omega)\hat{v}\hat{p}^*|$ is also shown for $R = 0.10$ (unfilled circles), $R = 0.50$ (unfilled diamonds) and $R = 1.00$ (unfilled squares). Results match the definition in (1.1).

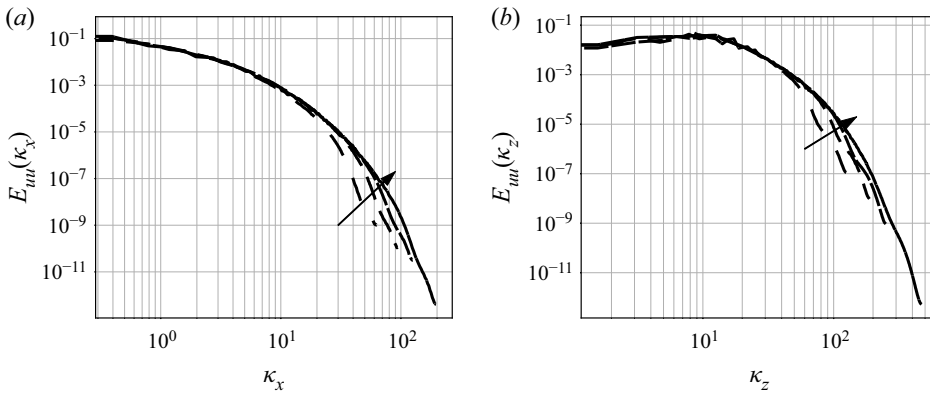


Figure 21. One-dimensional spectrum of streamwise velocity at $y^* \approx 15$ in $M_b = 6.00$ DNS case, with arrow showing increasing resolution ($N_x \times N_y \times N_z$): $320 \times 200 \times 240$, $480 \times 250 \times 360$, $640 \times 300 \times 480$ and $1000 \times 300 \times 600$.

Slight deviations in phase have been observed near the resonating frequency, which decrease as the wall permeability drops.

Appendix C. Turbulent channel flow over impermeable walls

The grid-refinement study is performed for the DNS case at $M_b = 6.00$ and the spatial spectra are given in figure 21. The two-point correlations are presented in figure 22. Two locations are selected to present the data: at $y^* \approx 15$ and the channel centre. The streamwise and spanwise correlations of velocity components all approach zero when the separation is close to half of the domain size in each direction, implying the satisfaction of the simulation box size. For the pressure correlation, all the data have a good decaying trend except in the spanwise direction at the channel centre plane, which gives a value

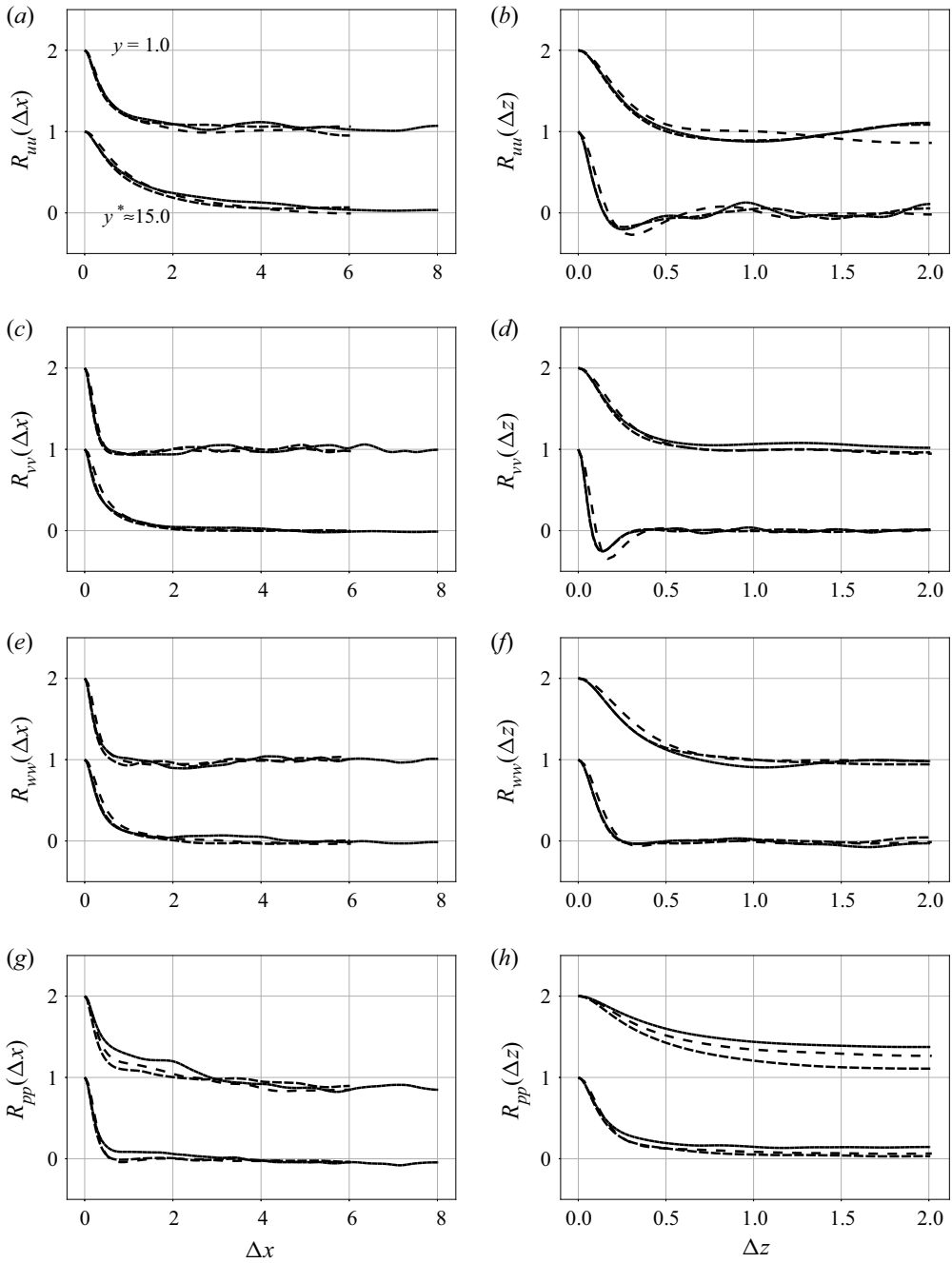


Figure 22. Two-point correlations in homogeneous directions of impermeable-wall cases at different Mach numbers: $M_b = 1.50$ (black dotted line), $M_b = 3.50$ (black dotted line), $M_b = 6.00$ (black solid line). Correlations are taken at channel centre $y = 1.0$ (shifted up) and buffer layer $y^* \approx 15$ for each Mach number.

around 0.1 near $\Delta z = 2$. By inspecting of the flow data, it is found that the fluctuation of pressure near the centre plane is very small, which causes the correlation curve to plateau.

Appendix D. Linear stability

D.1. Solver validation

The two-dimensional linearized Navier–Stokes equations and the equation of state, written in terms of the primitive variables are

$$\frac{\partial \rho'}{\partial t} + \frac{\partial \rho' \bar{u}_j}{\partial x_j} + \frac{\partial \bar{\rho} u'_j}{\partial x_j} = 0 \quad (\text{D1})$$

$$\begin{aligned} & \bar{\rho} \left(\frac{\partial u'_i}{\partial t} + \bar{u}_j \frac{\partial u'_i}{\partial x_j} + u'_j \frac{\partial \bar{u}_i}{\partial x_j} \right) + \rho' \bar{u}_j \frac{\partial \bar{u}_i}{\partial x_j} \\ &= -\frac{\partial p'}{\partial x_i} + \frac{1}{Re_a} \frac{\partial}{\partial x_j} \left[\bar{\mu} \left(\frac{\partial u'_i}{\partial x_j} + \frac{\partial u'_j}{\partial x_i} - \frac{2}{3} \delta_{ij} \frac{\partial u'_k}{\partial x_k} \right) + \mu' \left(\frac{\partial \bar{u}_i}{\partial x_j} + \frac{\partial \bar{u}_j}{\partial x_i} - \frac{2}{3} \delta_{ij} \frac{\partial \bar{u}_k}{\partial x_k} \right) \right] \end{aligned} \quad (\text{D2})$$

$$\begin{aligned} & \bar{\rho} \left(\frac{\partial T'}{\partial t} + \bar{u}_j \frac{\partial T'}{\partial x_j} + u'_j \frac{\partial \bar{T}}{\partial x_j} \right) + \rho' \bar{u}_j \frac{\partial \bar{T}}{\partial x_j} \\ &= (\gamma - 1) \left(\frac{\partial p'}{\partial t} + \bar{u}_j \frac{\partial p'}{\partial x_j} + u'_j \frac{\partial \bar{p}}{\partial x_j} \right) + \frac{1}{Pr Re_a} \frac{\partial}{\partial x_j} \left(\bar{k} \frac{\partial T'}{\partial x_j} + k' \frac{\partial \bar{T}}{\partial x_j} \right) \\ &+ \frac{\gamma - 1}{Re_a} \left\{ 2\bar{\mu} \left[\frac{\partial \bar{u}_k}{\partial x_j} \frac{\partial u'_k}{\partial x_j} + \frac{\partial \bar{u}_k}{\partial x_j} \frac{\partial u'_j}{\partial x_k} - \frac{2}{3} \frac{\partial \bar{u}_k}{\partial x_k} \frac{\partial u'_j}{\partial x_j} \right] \right. \\ &\left. + \mu' \left[\left(\frac{\partial \bar{u}_k}{\partial x_j} \right)^2 + \frac{\partial \bar{u}_k}{\partial x_j} \frac{\partial \bar{u}_j}{\partial x_k} - \frac{2}{3} \frac{\partial \bar{u}_k}{\partial x_k} \frac{\partial \bar{u}_j}{\partial x_j} \right] \right\} \end{aligned} \quad (\text{D3})$$

$$\rho' = \frac{p' \gamma}{\bar{T}} - \frac{\gamma \bar{p} \cdot T'}{\bar{T}^2} \quad (\text{D4})$$

Now, for clarity, the notation u, v, x, y is used. Assuming a perturbation in the form $\phi' = \hat{\phi}(y) \exp(i(\alpha x - \Omega t))$ and exploiting the spatial homogeneity of the base flow, the perturbed governing equations are given in terms of $\hat{u}, \hat{v}, \hat{p}, \hat{T}$ by

$$i\Omega \hat{p} - i\Omega \bar{p} \hat{T} / \bar{T} = i\alpha \bar{p} \hat{u} + \left(\bar{p} \frac{d}{dy} + \frac{\bar{T}}{\gamma} \frac{d\bar{\rho}}{dy} \right) \hat{v} + i\alpha \bar{u} \hat{p} - \frac{\bar{\rho} \bar{u}}{\gamma} \hat{T} \quad (\text{D5})$$

$$\begin{aligned} & -i\Omega \bar{\rho} \hat{u} - \frac{1}{Re_a} \left[\bar{\mu} \frac{d^2}{dy^2} + \frac{d\bar{\mu}}{d\bar{T}} \frac{d\bar{T}}{dy} \frac{d}{dy} \right] \hat{u} + \bar{\rho} \frac{d\bar{u}}{dy} \hat{v} \\ & - \frac{1}{Re_a} \left[\frac{d\bar{\mu}}{d\bar{T}} \frac{d^2 \bar{u}}{d\bar{T}^2} + \frac{d\bar{\mu}}{d\bar{T}} \frac{d\bar{u}}{dy} \frac{d}{dy} + \frac{d^2 \bar{\mu}}{d\bar{T}^2} \frac{d\bar{T}}{dy} \frac{d\bar{u}}{dy} \right] \hat{T} \\ &= - \left[i\alpha \bar{\rho} \bar{u} + \frac{4}{3} \frac{1}{Re_a} \bar{\mu} \alpha^2 \right] \hat{u} + \frac{i\alpha}{Re_a} \left[\frac{1}{3} \bar{\mu} \frac{d}{dy} + \frac{d\bar{\mu}}{d\bar{T}} \frac{d\bar{T}}{dy} \right] \hat{v} - i\alpha \hat{p} \end{aligned} \quad (\text{D6})$$

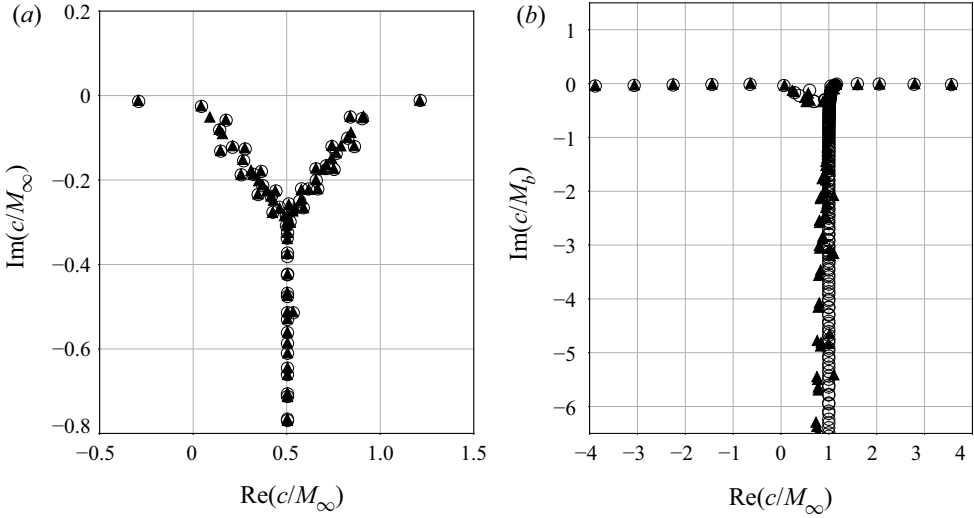


Figure 23. Complex wave speed of compressible Couette flow at $M_\infty = 2.0$, $Re_\infty = 2 \times 10^5$ (a) and supersonic channel flow at $M_b = 3.0$, $Re_b = 4880$ (b). Symbols are: (\blacktriangle) reference data from Hu & Zhong (1997) for (a) and Friedrich & Bertolotti (1997) for (b); (unfilled circles) data from current solver.

$$\begin{aligned}
 & -i\Omega \bar{\rho} \hat{v} - \frac{1}{Re_a} \frac{4}{3} \left[\bar{\mu} \frac{d^2}{dy^2} + \frac{d\bar{\mu}}{d\bar{T}} \frac{d\bar{T}}{dy} \frac{d}{dy} \right] \hat{v} + \frac{d\hat{p}}{dy} \\
 & = \frac{i\alpha}{Re_a} \left[\frac{1}{3} \bar{\mu} \frac{d}{dy} - \frac{2}{3} \frac{d\bar{\mu}}{d\bar{T}} \frac{d\bar{T}}{dy} \right] \hat{u} - \left[i\alpha \bar{\rho} \hat{u} + \frac{1}{Re_a} \bar{\mu} \alpha^2 \right] \hat{v} + \frac{i\alpha}{Re_a} \frac{d\bar{\mu}}{d\bar{T}} \frac{d\bar{T}}{dy} \hat{T} \quad (D7)
 \end{aligned}$$

$$\begin{aligned}
 & (\gamma - 1) i\Omega \hat{p} - i\Omega \bar{p} \hat{T} - \frac{2(\gamma - 1) \bar{\mu}}{Re_a} \frac{d\bar{u}}{dy} \frac{d\hat{u}}{dy} + \bar{\rho} \frac{d\bar{T}}{dy} \hat{v} \\
 & - \frac{1}{Pr Re_a} \left[\bar{k} \frac{d^2}{dy^2} + 2 \frac{d\bar{k}}{d\bar{T}} \frac{d\bar{T}}{dy} \frac{d}{dy} + \frac{d^2 \bar{k}}{d\bar{T}^2} \left(\frac{d\bar{T}}{dy} \right)^2 + \frac{d\bar{k}}{d\bar{T}} \frac{d^2 \bar{T}}{dy^2} \right] \hat{T} - \frac{(\gamma - 1) d\bar{\mu}}{Re_a} \frac{d\bar{T}}{dy} \left(\frac{d\bar{u}}{dy} \right)^2 \hat{T} \\
 & = i\alpha \frac{2(\gamma - 1)}{Re_a} \bar{\mu} \frac{d\bar{u}}{dy} \hat{v} + i\alpha (\gamma - 1) \bar{u} \hat{p} - \left[i\alpha \bar{\rho} \hat{u} + \frac{1}{Pr Re_a} \bar{k} \alpha^2 \right] \hat{T}. \quad (D8)
 \end{aligned}$$

Note that the perturbation of dynamic viscosity and thermal conductivity is related to the perturbed temperature via

$$\mu' = \frac{d\bar{\mu}}{d\bar{T}} T', \quad k' = \frac{d\bar{k}}{d\bar{T}} T'. \quad (D9a,b)$$

The above equations are solved at Gauss–Lobatto–Chebyshev points. To validate the solver, a supersonic Couette flow case from Hu & Zhong (1997) and the supersonic channel flow case from Friedrich & Bertolotti (1997) are tested and compared to the literature, as shown in figure 23. Good agreement has been achieved for both cases.

REFERENCES

- ABDERRAHMAN-ELENA, N. & GARCÍA-MAYORAL, R. 2017 Analysis of anisotropically permeable surfaces for turbulent drag reduction. *Phys. Rev. Fluids* **2** (11), 114609.

- AKSELVOLL, K. & MOIN, P. 1995 Large eddy simulation of turbulent confined co-annular jets and turbulent flow over a backward facing step. *Rep. TF-63*, Thermo-sciences Division, Department of Mechanical Engineering, Stanford University, CA 94395.
- AURÉGAN, Y. & LEROUX, M. 2008 Experimental evidence of an instability over an impedance wall in a duct with flow. *J. Sound Vib.* **317** (3–5), 432–439.
- AURÉGAN, Y., LEROUX, M. & PAGNEUX, V. 2005 Abnormal behavior of an acoustical liner with flow. In *Forum Acusticum 2005, Budapest*.
- BEAM, R.M. & WARMING, R.F. 1978 An implicit factored scheme for the compressible Navier–Stokes equations. *AIAA J.* **16** (4), 393–402.
- BEAM, R.M. & WARMING, R.F. 1976 An implicit finite-difference algorithm for hyperbolic systems in conservation-law form. *J. Comput. Phys.* **22** (1), 87–110.
- BRAMBLEY, E.J. 2009 Fundamental problems with the model of uniform flow over acoustic linings. *J. Sound Vib.* **322** (4–5), 1026–1037.
- BRANDES, M. & RONNEBERGER, D. 1995 Sound amplification in flow ducts lined with a periodic sequence of resonators. In *CEAS/AIAA Joint Aeroacoustics Conference, 1st, Munich, Germany*, pp. 893–901.
- CESS, R.D. 1958 A survey of the literature on heat transfer in turbulent tube flow. *Res. Rep.* pp. 8–0529.
- CHAPELIER, J.-B., WASISTHO, B. & SCALO, C. 2018 A coherent vorticity preserving eddy-viscosity correction for large-eddy simulation. *J. Comput. Phys.* **359**, 164–182.
- CHAPELIER, J.-B., WASISTHO, B. & SCALO, C. 2019 Large-eddy simulation of temporally developing double helical vortices. *J. Fluid Mech.* **863**, 79–113.
- DEL ALAMO, J.C. & JIMENEZ, J. 2006 Linear energy amplification in turbulent channels. *J. Fluid Mech.* **559**, 205–213.
- DOUASBIN, Q., SCALO, C., SELLE, L. & POINSOT, T. 2018 Delayed-time domain impedance boundary conditions (D-TDIBC). *J. Comput. Phys.* **371**, 50–66.
- DRAGNA, D., PINEAU, P. & BLANC-BENON, P. 2015 A generalized recursive convolution method for time-domain propagation in porous media. *J. Acoust. Soc. Am.* **138** (2), 1030–1042.
- DUAN, L., BEEKMAN, I. & MARTIN, M.P. 2010 Direct numerical simulation of hypersonic turbulent boundary layers. Part 2. Effect of wall temperature. *J. Fluid Mech.* **655**, 419–445.
- FEDOROV, A. 2011 Transition and stability of high-speed boundary layers. *Annu. Rev. Fluid Mech.* **43**, 79–95.
- FEDOROV, A., SHIPLYUK, A., MASLOV, A., BUROV, E. & MALMUTH, N. 2003 Stabilization of a hypersonic boundary layer using an ultrasonically absorptive coating. *J. Fluid Mech.* **479**, 99–124.
- FEDOROV, A.V., KOZLOV, V.F., SHIPLYUK, A.N., MASLOV, A.A. & MALMUTH, N.D. 2006 Stability of hypersonic boundary layer on porous wall with regular microstructure. *AIAA J.* **44** (8), 1866–1871.
- FRIEDRICH, R. & BERTOLOTI, F.P. 1997 Compressibility effects due to turbulent fluctuations. *Appl. Sci. Res.* **57**, 165–194.
- FUNG, K.Y. & JU, H. 2001 Broadband time-domain impedance models. *AIAA J.* **39** (8), 1449–1454.
- FUNG, K.-Y. & JU, H. 2004 Time-domain impedance boundary conditions for computational acoustics and aeroacoustics. *Intl J. Comput. Fluid Dyn.* **18** (6), 503–511.
- FUNG, K.-Y., JU, H. & TALLAPRAGADA, B. 2000 Impedance and its time-domain extensions. *AIAA J.* **38** (1), 30–38.
- HU, S. & ZHONG, X. 1997 Linear instability of compressible plane Couette flows. In *AIAA Aerospace Sciences Meeting and Exhibit, Reno, NV, AIAA Paper 1997-432*.
- HUANG, P.G., COLEMAN, G.N. & BRADSHAW, P. 1995 Compressible turbulent channel flows: DNS results and modelling. *J. Fluid Mech.* **305** (1), 185–218.
- HUNT, J.C.R., WRAY, A.A. & MOIN, P. 1988 Eddies, streams, and convergence zones in turbulent flows. In *Center for Turbulence Research, Rept. CTR-S88, Stanford, CA*, pp. 193–208.
- INGARD, U. 1959 Influence of fluid motion past a plane boundary on sound reflection, absorption, and transmission. *J. Acoust. Soc. Am.* **31** (7), 1035–1036.
- JIMÉNEZ, J., UHLMANN, M., PINELLI, A. & KAWAHARA, G. 2001 Turbulent shear flow over active and passive porous surfaces. *J. Fluid Mech.* **442**, 89–117.
- JOSEPH, R.M., HAGNESS, S.C. & TAFLOVE, A. 1991 Direct time integration of Maxwell’s equations in linear dispersive media with absorption for scattering and propagation of femtosecond electromagnetic pulses. *Opt. Lett.* **16** (18), 1412–1414.
- KINSLER, L.E., FREY, A.R., COPPENS, A.B. & SANDERS, J.V. 1999 *Fundamentals of Acoustics*, 4th edn. Wiley.
- LEE, M. & MOSER, R.D. 2015 Direct numerical simulation of turbulent channel flow up to $Re_\tau = 5200$. *J. Fluid Mech.* **774**, 395–415.
- LIN, J., SCALO, C. & HESSELINK, L. 2016 High-fidelity simulation of a standing-wave thermoacoustic–piezoelectric engine. *J. Fluid Mech.* **808**, 19–60.

- MALIK, M.L. 1990 Numerical methods for hypersonic boundary layer stability. *J. Comput. Phys.* **86**, 376–413.
- MARX, D., AURÉGAN, Y., BAILLIET, H. & VALIÈRE, J.-C. 2010 PIV and LDV evidence of hydrodynamic instability over a liner in a duct with flow. *J. Sound Vib.* **329** (18), 3798–3812.
- MYERS, M.K. 1980 On the acoustic boundary condition in the presence of flow. *J. Sound Vib.* **71** (3), 429–434.
- NAGARAJAN, S. 2004 Leading edge effects in bypass transition. PhD thesis, Stanford University.
- NAGARAJAN, S., LELE, S.K. & FERZIGER, J.H. 2003 A robust high-order compact method for large eddy simulation. *J. Comput. Phys.* **191**, 392–419.
- OLIVETTI, S., SANDBERG, R.D. & TESTER, B.J. 2015 Direct numerical simulation of turbulent flow with an impedance condition. *J. Sound Vib.* **344**, 28–37.
- ÖZYÖRÜK, Y. & LONG, L.N. 1997 A time-domain implementation of surface acoustic impedance condition with and without flow. *J. Comput. Acoust.* **5** (3), 277–296.
- ÖZYÖRÜK, Y., LONG, L.N. & JONES, M.G. 1998 Time-domain numerical simulation of a flow-impedance tube. *J. Comput. Phys.* **146**, 29–57.
- PATEL, D.I., GUPTA, P. & SCALO, C. 2017 Surface impedance determination via numerical resolution of the inverse Helmholtz problem. In *23rd AIAA/CEAS Aeroacoustics Conference, AIAA Paper 2017-3695*.
- POPE, S.B. 2000 *Turbulent Flows*. Cambridge University Press.
- PUJALS, G., GARCÍA-VILLALBA, M., COSSU, C. & DEPARDON, S. 2009 A note on optimal transient growth in turbulent channel flows. *Phys. Fluids* **21** (1), 015109.
- PULLIAM, T.H. & CHAUSSEE, D.S. 1981 A diagonal form of an implicit approximate-factorization algorithm. *J. Comput. Phys.* **39** (2), 347–363.
- RAHBARI, I. & SCALO, C. 2017 Linear stability analysis of compressible channel flow over porous walls. In *Whither Turbulence and Big Data in the 21st Century?* (ed. A. Pollard, L. Castillo, L. Danaila & M. Glauser), pp. 451–467. Springer.
- RASHEED, A., HORNUNG, H.G., FEDOROV, A.V. & MALMUTH, N.D. 2002 Experiments on passive hypervelocity boundary-layer control using an ultrasonically absorptive surface. *AIAA J.* **40** (3), 481–489.
- RAUPACH, M.R., ANTONIA, R.A. & RAJAGOPALAN, S. 1991 Rough-wall turbulent boundary layers. *Appl. Mech. Rev.* **40** (1), 1–25.
- REYNOLDS, W.C. & HUSSAIN, A.K.M.F. 1972 The mechanics of an organized wave in turbulent shear flow. Part 3. Theoretical models and comparisons with experiments. *J. Fluid Mech.* **54** (2), 263–288.
- REYNOLDS, W.C. & TIEDERMAN, W.G. 1967 Stability of turbulent channel flow, with application to Malkus's theory. *J. Fluid Mech.* **27** (2), 253–272.
- RIENSTRA, S. 2006 Impedance models in time domain, including the extended Helmholtz resonator model. In *12th AIAA/CEAS Aeroacoustics Conference (27th AIAA Aeroacoustics Conference)*, AIAA Paper 2006-2686.
- RIENSTRA, S.W. & DARAU, M. 2011 Boundary-layer thickness effects of the hydrodynamic instability along an impedance wall. *J. Fluid Mech.* **671**, 559–573.
- RINALDI, E., PATEL, A., SCHLATTER, P. & PECNIK, R. 2017 Linear stability of buffer layer streaks in turbulent channels with variable density and viscosity. *Phys. Rev. Fluids* **2** (11), 113903.
- ROSTI, M.E., BRANDT, L. & PINELLI, A. 2018 Turbulent channel flow over an anisotropic porous wall – drag increase and reduction. *J. Fluid Mech.* **842**, 381–394.
- ROTTA, J.C. 1960 *Turbulent Boundary Layers with Heat Transfer in Compressible Flow*. Advisory Group for Aeronautical Research and Development.
- SCALO, C., BODART, J. & LELE, S.K. 2015 Compressible turbulent channel flow with impedance boundary conditions. *Phys. Fluids* **27**, 035107.
- SEBASTIAN, R., MARX, D. & FORTUNÉ, V. 2019 Numerical simulation of a turbulent channel flow with an acoustic liner. *J. Sound Vib.* **456**, 306–330.
- SOSA, V.C.B., PATEL, D., CHAPÉLIER, J.-B., WARTEMAN, V., WAGNER, A. & SCALO, C. 2019 Numerical investigation of second-mode attenuation over carbon/carbon porous surfaces. *J. Spacecr. Rockets* **56** (2), 319–332.
- SQUIRE, D.T., MORRILL-WINTER, C., HUTCHINS, N., SCHULTZ, M.P., KLEWICKI, J.C. & MARUSIC, I. 2016 Comparison of turbulent boundary layers over smooth and rough surfaces up to high Reynolds numbers. *J. Fluid Mech.* **795**, 210–240.
- TAM, C.K.W. & AURIAULT, L. 1996 Time-domain impedance boundary conditions for computational aeroacoustics. *AIAA J.* **34** (5), 917–923.
- TESTER, B.J. 1973 The propagation and attenuation of sound in lined ducts containing uniform or ‘plug’ flow. *J. Sound Vib.* **28** (2), 151–203.
- TRETTEL, A. & LARSSON, J. 2016 Mean velocity scaling for compressible wall turbulence with heat transfer. *Phys. Fluids* **28**, 026102.

Trapped waves in high-speed turbulent flow over porous walls

- TROIAN, R., DRAGNA, D., BAILLY, C. & GALLAND, M.-A. 2017 Broadband liner impedance reduction for multimodal acoustic propagation in the presence of a mean flow. *J. Sound Vib.* **392**, 200–216.
- ULERICH, R.D. 2014 Reducing turbulence-and transition-driven uncertainty in aerothermodynamic heating predictions for blunt-bodied reentry vehicles. PhD thesis, University of Texas at Austin.
- VREMAN, A.W. 2004 An eddy-viscosity subgrid-scale model for turbulent shear flow: algebraic theory and applications. *Phys. Fluids* **16** (10), 3670.
- WAGNER, A. 2014 Passive hypersonic boundary layer transition control using ultrasonically absorptive carbon-carbon ceramic with random microstructure. PhD thesis, Katholieke Universiteit, Leuven.
- WILCOX, D.C. 1998 *Turbulence Modeling for CFD*, 3rd edn. DCW Industries.
- ZHAO, R., LIU, T., WEN, C.Y., ZHU, J. & CHENG, L. 2018 Theoretical modeling and optimization of porous coating for hypersonic laminar flow control. *AIAA J.* **56** (8), 2942–2946.